Check for updates

Article

SOURCE DATA | TRANSPARENT PROCESS

THE EMBO JOURNAL

Keratin filaments mediate the expansion of extra-embryonic membranes in the post-gastrulation mouse embryo

Wallis Nahaboo[1], Sema Elif Eski[1], Evangéline Despin-Guitard[1], Marjorie Vermeersch[2], Marie Versaevel[3], Bechara Saykali[1,†], Daniel Monteyne[2], Sylvain Gabriele[3], Thomas M Magin[4], Nicole Schwarz[5], Rudolf E Leube[5], An Zwijsen[6], David Perez-Morga[2,7], Sumeet Pal Singh[1] & Isabelle Migeotte[1,*]

Abstract

Mesoderm arises at gastrulation and contributes to both the mouse embryo proper and its extra-embryonic membranes. Two-photon live imaging of embryos bearing a keratin reporter allowed recording filament nucleation and elongation in the extra-embryonic region. Upon separation of amniotic and exocoelomic cavities, keratin 8 formed apical cables co-aligned across multiple cells in the amnion, allantois, and blood islands. An influence of substrate rigidity and composition on cell behavior and keratin content was observed in mesoderm explants. Embryos lacking all keratin filaments displayed a deflated extra-embryonic cavity, a narrow thick amnion, and a short allantois. Single-cell RNA sequencing of sorted mesoderm cells and micro-dissected amnion, chorion, and allantois, provided an atlas of transcriptomes with germ layer and regional information. It defined the cytoskeleton and adhesion expression profile of mesoderm-derived keratin 8-enriched cells lining the exocoelomic cavity. Those findings indicate a novel role for keratin filaments in the expansion of extra-embryonic structures and suggest mechanisms of mesoderm adaptation to the environment.

Keywords extra-embryonic membranes; gastrulation; intermediate filaments; live imaging; mouse embryo

Subject Categories Cell Adhesion, Polarity & Cytoskeleton; Development

DOI 10.15252/embj.2021108747 | Received 18 May 2021 | Revised 21 January 2022 | Accepted 24 January 2022

The EMBO Journal (2022) e108747

Introduction

Prior to gastrulation, mammalian embryos absorb nutrients through endocytosis. Further development depends on extra-embryonic (ExE) tissues (Fig 1A): the amnion protects the embryo while the yolk sac, umbilical cord, and placenta provide water, nutrients, and gas exchange (Roberts *et al*, 2016). The fetal portion of the placenta comprises trophoblastic, mesenchymal, and vascular cells. Trophoblasts originate from trophectoderm, the outer layer of the blastocyst, that solely contributes to ExE structures including ectoplacental cone and ExE ectoderm (Arnold & Robertson, 2009; Nahaboo & Migeotte, 2018). Mesenchymal and vascular cells originate from the epiblast, a derivative of the blastocyst inner cell mass that is the precursor for most embryonic tissues. During mouse embryo gastrulation, posterior epiblast cells delaminate at the primitive streak to become endoderm or mesoderm. ExE mesoderm emerges from the proximal part of the streak and accumulates between ExE ectoderm and visceral endoderm to create the amniochorionic fold, in which fusion of multiple lumens generates the exocoelomic cavity (Pereira *et al*, 2011). Amnion is a thin bilayer of epiblast-derived ectoderm and ExE mesoderm that separates exocoelomic and amniotic cavities (Dobreva *et al*, 2018). When the amniochorionic fold is fully expanded, chorionic walls made of ExE ectoderm and mesoderm fuse anteriorly (Pereira *et al*, 2011). The allantois, precursor for the umbilical cord (Inman & Downs, 2007), is an ExE mesoderm bud continuous with the primitive streak that grows toward the chorion, to which it attaches around embryonic day (E) 8.5 (Inman & Downs, 2006). Placenta arises from the fusion of the ectoplacental cone, chorion, and allantois (Watson & Cross, 2005). The fetus becomes dependent on the interaction of maternal

1 Institut de Recherche Interdisciplinaire en Biologie Humaine et Moléculaire (IRIBHM), Université Libre de Bruxelles, Brussels, Belgium
2 Center for Microscopy and Molecular Imaging (CMMI), Université Libre de Bruxelles, Gosselies, Belgium
3 Mechanobiology and Soft Matter Group, Research Institute for Biosciences, University of Mons, Mons, Belgium
4 Division of Cell & Developmental Biology, Institute of Biology, Leipzig University, Leipzig, Germany
5 Institute of Molecular and Cellular Anatomy, RWTH Aachen University, Aachen, Germany
6 KU Leuven, Leuven, Belgium
7 Laboratory of Molecular Parasitology, IBMM, Université Libre de Bruxelles, Gosselies, Belgium
*Corresponding author. Tel: +32 25556430; E-mail: isabelle.migeotte@ulb.be
†Present address: Laboratory of Genome Integrity, National Cancer Institute, NIH, Bethesda, MD, USA

© 2022 The Authors

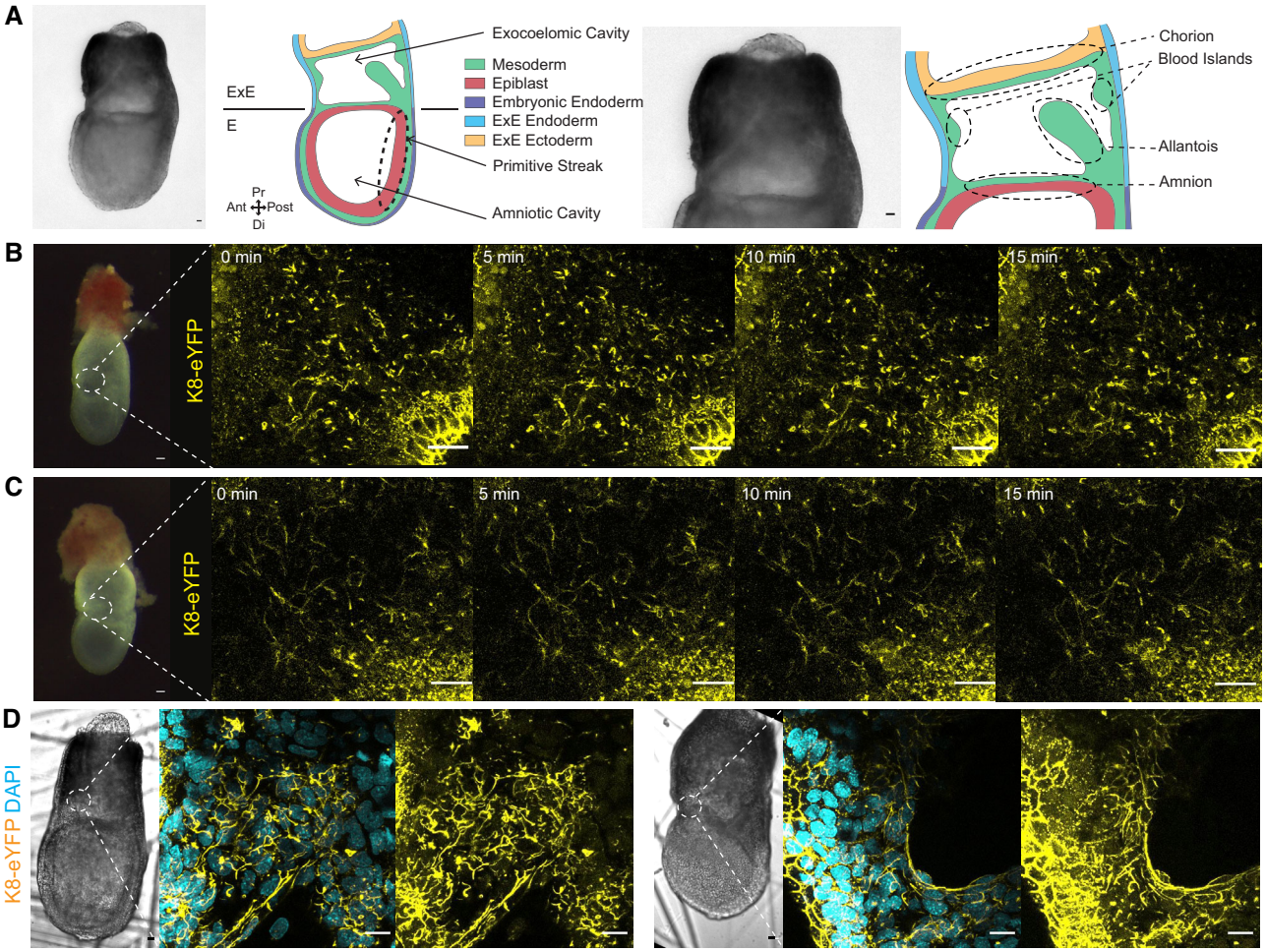


Figure 1. Nucleation of K8 filaments in E7.5 mouse embryo.

A Bright-field picture and scheme of an E7.5 Late Bud (LB) embryo showing germ layers in Embryonic (E) and Extra-Embryonic (ExE) regions (Left). Zoom on ExE region with annotations of ExE structures (Right).

B Bright-field picture of a 0B K8-eYFP embryo (Left) and time series of two-photon live imaging of ExE region (Right). Time interval is 5 min (n = 3).

C Bright-field picture of EB K8-eYFP embryo (Left) and time series of two-photon live imaging of ExE region (Right). Time interval is 5 min (n = 4).

D Bright-field pictures of K8-eYFP LB embryos (n = 30), and high magnification spectral acquisition of areas of ExE mesoderm corresponding to dashed white areas. K8-eYFP and DAPI appear in yellow and cyan, respectively.

Data information: Scale bars represent 25 μm, except for bright-field pictures in (B, C) where scale bars show 50 μm.

and fetal circulations in the placental labyrinth from E10.5 (Burton *et al*, 2016; Soares *et al*, 2018).

To adapt to embryonic growth and needs, ExE tissues need to rapidly expand and change morphology. At E8.5 the U-shaped embryo turns along its dorsoventral axis and becomes enclosed in the amniotic sac, which is surrounded by the yolk sac. The umbilical cord accommodates fetal movements and ensures maintenance of blood flow between fetus and placenta. Therefore, the amnion, yolk sac, and allantois must be both resistant and elastic. Among cytoskeletal components, intermediate filaments display the highest tensile strength and toughness, as well as remarkable elasticity, which allow cells to sustain and recover from large deformations (Loschke *et al*, 2015). As we found high expression of intermediate filament components keratins (Krt or K) 8 and 18 in ExE mesoderm (Saykali *et al*, 2019), we set up to explore keratin filament organization and function in mesoderm-derived ExE membranes around gastrulation.

Krt intermediate filaments (KF) are formed of obligatory heterodimers of type I and type II monomers, assembled into tetramers that associate to generate 8–12 nm filaments (Loschke *et al*, 2015). In epithelial tissues, desmosome-anchored KF form a mechanically resilient transcellular network that is modulated by physical stress (Moch *et al*, 2020). In the mouse embryo, K8 and 18 are already detected in a subset of cells at the eight-cell stage (Lu *et al*, 2005), and it was suggested that they function as asymmetrically inherited factors that specify the first trophectoderm cells (Lim *et al*, 2020). Establishment of a knock-in K8-eYFP fusion mouse line allowed tracking KF network formation and dynamics in live embryos without functional alteration (Schwarz *et al*, 2015). K8-eYFP accumulates as dots at cell borders during

 © 2022 The Authors

the morula stage (Moch *et al*, 2020). At the blastocyst stage, there is a dense KF network in trophectoderm, whereas the inner cell mass is devoid of K8/18. At E7, immunostaining for K8 marks ExE ectoderm and mesoderm, as well as visceral endoderm (Saykali *et al*, 2019). An important role for KF in mesenchymal tissue was uncovered in the frog embryo, where KF mechanically connect mesendodermal cells and are required for their efficient collective migration (Sonavane *et al*, 2017).

Because of high and ubiquitous K8 expression in ExE cells, we used the K8-eYFP line to record both the distribution of KF and the morphogenesis of ExE tissues, through two-photon live microscopy. At late gastrulation stage, live imaging identified KF nucleation and elongation in the amnion, allantois, chorion, and blood islands. All tissues in contact with the rapidly expanding exocoelomic cavity, presumably exposed to the highest mechanical constraint, displayed long KF cables connecting several cells. Culture of embryonic and ExE mesoderm explants on various substrates showed that cell speed and KF content depend on the rigidity and composition of the matrix. Mutant embryos devoid of all keratins had a collapsed ExE cavity, a short thick amnion, and a small allantois, suggesting KF play a major role in shaping ExE membranes. As profiles of early ExE tissues at cellular resolution were lacking from mouse embryo single-cell atlas, we performed single-cell RNA sequencing analysis (scRNA-seq) of E7.25 mesoderm cells as well as E7.75 micro-dissected amnion, allantois, and chorion, thereby identifying the expression landscape of KF-rich epithelial and mesenchymal cells and providing a detailed atlas of ExE structures.

Results

KF form a coordinated network across multiple cells in ExE mesoderm

To record KF dynamics in the post-implantation mouse embryo, we performed two-photon static and live imaging of *ex vivo* cultured K8-eYFP embryos from the Early Streak (ES, E6.25) to the Late Bud/Neural Plate (LB/NP, E7.75) stages (Downs & Davies, 1993) (Schwarz *et al*, 2015) (Fig 1A, Appendix Fig S1A). As expected, eYFP was present in visceral endoderm, ExE ectoderm, and ExE mesoderm (Appendix Fig S1B and C). 3D-reconstruction of LB embryos stained for F-actin showed that, similar to E7.25 ExE mesoderm (Saykali *et al*, 2019), ExE mesenchyme in amnion, chorion, and allantois had low F-actin, compared to embryonic mesoderm (Appendix Fig S1D and Movie EV1). From the Late Streak/Zero Bud (LS/0B) stages, eYFP-positive dots (5.34 ± 0.62 μm², $n = 24$ from six embryos, Table 1) could be detected specifically in ExE mesoderm cells (Fig 1B, Appendix Fig S1C and Movie EV2). Dots subsequently elongated into filamentous particles up to 25 μm in length (24.76 ± 2.47 μm, $n = 19$ from eight embryos, Table 1) and organized a reticular web (Fig 1C and Movie EV3). Higher resolution imaging of Early Bud (EB) to NP fixed samples showed that K8 containing filaments could form linear structures up to 75 μm in length (65 ± 11.92 μm, $n = 11$ from six embryos, Table 1) continuous across multiple cells, in the borders of the expanding ExE cavity (Fig 1D and Movie EV4).

Table 1. Summary of the dimensions of the eYFP-positive dots, filamentous particles and filaments at the Late Streak/Zero Bud, Early Bud and Neural Plate stages.

Mean	K8-eYFP dots-area (μm²)	K8-eYFP filamentous particles-length (μm)	K8-eYFP linear structures (μm)
Number of values	24	19	11
Mean	5.34	24.76	64.99
Lower 95% CI of mean	4.722	22.29	53.07
Upper 95% CI of mean	5.958	27.22	76.91
Confident interval	0.618	2.46	11.92

Source data are available online for this Table.

Stretchable KF-rich cables connect amnion, exocoelomic wall, and chorion

Live imaging of K8-eYFP embryos recorded the global morphogenetic events that shape ExE structures (Fig 2). The amnion displayed small KF bundles perpendicular to its ExE surface. We noticed the formation of stable (> 3 h) K8 containing "cables", mostly in the anterior part of the embryo, bridging the mesoderm-derived part of the amnion and the wall of the exocoelomic cavity (Fig 2A and Movie EV5). Those cables stretched progressively (initial length 52.61 ± 15.37 μm and width 9.69 ± 5.8 μm, final length 130.5 ± 48.98 μm and width 5 ± 3.41 μm, $n = 5$, Table 2) and finally snapped as the cavity grew; they likely represent remnants of connections between amnion mesoderm and blood islands that break upon amnion closure. Cables linking amnion and wall were not detected in fixed samples, suggesting they might be unstable and lost upon fixation. In a subset of embryos ($n = 6$ with the adequate stage and orientation), a larger KF-rich structure was visible in the anterior region (Fig 2B and Movie EV6), corresponding to the chorion portion of the amniochorionic fold. It grew longer and thinner before rupturing at the Anterior Separation Point (Appendix Fig S1A) (Pereira *et al*, 2011), allowing full expansion of the exocoelomic cavity and positioning of the chorion close to the ectoplacental cone.

KF form a cage around the allantois

The allantois grew steadily toward the chorion. It had an irregular shape and developed smooth bulges particularly at its distal extremity. K8-eYFP uncovered a striking difference between the external layer of the allantois, which has been referred to as "mesothelium" (Daane *et al*, 2011) and is called "cortex" in this study, and the inner allantois cells: the cortex displayed a rich KF network, while inner allantois cells had a lower KF content (Fig 2C and D and Movie EV7). 3D reconstruction from whole-mount imaging of fixed samples illustrated the dense reticular network covering the allantois as well as the ExE side of the amnion and the retracting chorion (Fig 2E, E′ and E″ and Movies EV8 and EV9). Interestingly, the allantois cortex displayed KF-rich cell blebs (as described in (Daane *et al*, 2011)), some of which were directed toward reciprocal blebs in chorion mesenchyme (Fig 2E). Comparing sections from K8-eYFP

© 2022 The Authors

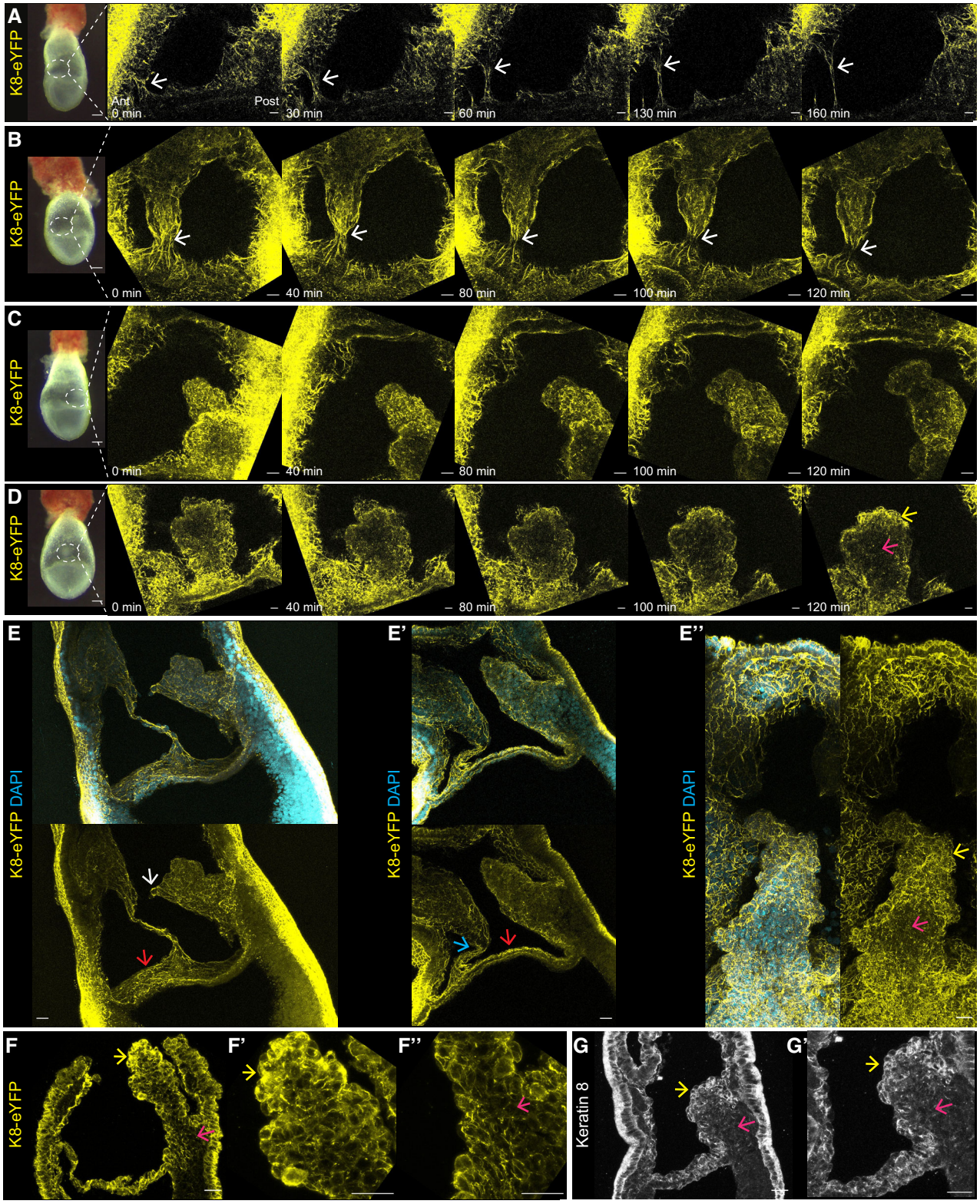


Figure 2.

© 2022 The Authors

Figure 2. K8 filaments extend in the ExE region.

A–D Bright-field pictures of K8-eYFP (Left) and Z-projections of time series (Right) of live LB K8-eYFP embryos imaged using two-photon laser with time intervals between 20 and 30 min, focusing on regions corresponding to dashed white areas. (A) Lateral view showing extension of K8 containing cables (white arrows) attached to the amnion and ExE wall (n = 10). (B) Anterior view showing chorion retraction at the Anterior Separation Point (white arrows) (n = 6). (C) Lateral and (D) Posterior views showing allantois growth over time (n = 12 and 3). Allantois cortex and mesenchyme are indicated with yellow and magenta arrows, respectively.

E–E″ Spectral images at high magnification of ExE region from fixed K8-eYFP LB/NP embryos (n = 20). (E) lateral view where white arrows point to allantois edge and red arrows to amnion. (E′) lateral view where blue arrow shows Anterior Separation Point and red arrow the amnion. (E″) posterior view focused on allantois where yellow arrow indicates allantois cortex and magenta arrow the mesenchyme. K8-eYFP appears in yellow and DAPI in cyan.

F–F″ Immunostaining on sagittal section (anterior to the left) of a LB K8-eYFP embryo (n = 20) stained with anti-eGFP antibody (yellow), focusing on ExE region (F); higher magnification images of allantois edge (F′, yellow arrow) and base (F″, magenta arrow).

G, G′ Immunostaining on sagittal section of a LB wild-type embryo (n = 32) stained with anti-Krt8 antibody (white) (G); higher magnification acquisition centered on allantois (G′) where yellow arrows indicate allantois cortex and magenta arrows point to allantois mesenchyme.

Data information: Scale bars represent 25 μm, except for bright-field pictures in (A–D) where scale bars show 100 μm.

Table 2. Summary of cables dimensions recorded from live imaging of K8eYFP embryos

	K8-eYFP-live-min length (μm)	K8-eYFP-live-max length (μm)	K8-eYFP-live-min thickness (μm)	K8-eYFP-live-max thickness (μm)
Number of values	5	5	5	5
Mean	52.61	130.5	4.99	9.686
Lower 95% CI of mean	37.24	81.52	1.584	3.879
Upper 95% CI of mean	67.98	179.5	8.396	15.49
Confident interval	15.37	49	3.406	5.804

Source data are available online for this Table.

embryos (Fig 2F, F′ and F″) and wild-type embryo sections immunostained for K8 (Fig 2G and G′) confirmed that K8-eYFP fusion protein recapitulates native K8 expression pattern.

ExE cell populations have distinct morphological characteristics

Scanning electron microscopy (SEM) of LB/NP embryos provided complementary information on ExE tissues morphology (Fig 3A). Blood islands were distinguished on the cavity wall, notably through the emergence of tubular structures (Fig 3B). The allantois had a "cotton candy" appearance (Fig 3C) (Daane *et al*, 2011). Allantois cortex consisted of a cohesive layer of stretched cells with short villi (Fig 3C′). In contrast, inside cells were rounder; they displayed long entangled filopodia mostly concentrated at cell–cell junctions and a network of twisty, branched filaments (Fig 3D, and zoom in E and E′). In the amnion, SEM highlighted the difference between mostly flat epiblast-derived cells at the embryonic side (Fig 3F) and mesoderm-derived cells forming a cobblestone landscape at the ExE side (Fig 3G and G′). Transmission electron microscopy (TEM) uncovered subcellular details, such as filaments and adhesion complexes. In blastocyst trophectoderm, KF nucleation sites co-localize with nascent desmosomes (Moch *et al*, 2020). In the allantois (Fig 3H–J), we found tight and adherens junctions in inner cells (Fig 3I and I′), whereas external cells were predominantly connected by adherens junctions (Fig 3J). Microfilaments adjacent to adherens junctions were detected at higher magnification (Fig 3J′). In the amnion (Fig 3K–M), tight and adherens junctions were found in epiblast (Fig 3L)- and mesoderm (Fig 3M and M′)-derived cells. In addition, atypical, possibly immature, desmosome-like junctions were observed (Fig 3L′). Filament bundles and desmosomes were abundant in chorion (Fig 3N and N′). Interestingly, TEM unveiled the presence of primary cilia specifically in cuboidal cells on the posterior side of the allantois base, where high and localized Hedgehog signaling was previously identified through a *Ptc1*:lacZ reporter (Daane & Downs, 2011) (Fig 3O and O′). Those cells displayed nascent desmosomes (Fig 3O″), compatible with their lower permeability to dextran (Daane *et al*, 2011).

Embryos lacking keratin display major defects in ExE structures

Due to redundancy among keratins, it is difficult to interpret phenotypes resulting from knocking out individual keratin genes. Deletion of *K8* provokes an embryonic lethal phenotype at E12.5 associated with a defect in placenta maturation (Baribault *et al*, 1993). Combined deletions of *K18/K19* (Hesse *et al*, 2000) or *K8/K19* (Tamai *et al*, 2000) causes fragility of giant trophoblast cells and extensive hemorrhages, which leads to death at E10. As KF assembly relies on obligate heterodimerization of members of each of the two families, deletion of the whole keratin family cluster II plus the flanking type I *K18* ($KtyII^{-/-}$) allows to fully overcome redundancy and leads to growth retardation from E8.5. Mutant embryos arrest around E9.5 and display multiple yolk sac defects (Vijayaraj *et al*, 2009, 2010). To explore the function of keratin in ExE mesoderm-derived structures, we examined keratin-depleted embryos at earlier stages of development.

$KtyII^{-/-}$ embryos displayed specific phenotypes as early as E7.5 (Figs 4A and EV1A): the ExE region appeared disorganized, with a narrow cavity and scrambled tissue architecture. Up to E8.5, the severity of the phenotype was variable (Fig EV1B and C), suggesting other cytoskeletal components, such as vimentin, might partially compensate for the loss of keratins. Nonetheless, all mutant embryos arrested around E9 (Fig EV1D). Immunostaining for K8 confirmed the absence of the protein (Figs 4B and EV1C). There was no difference in the expression patterns of F-actin, vimentin, E-cadherin, and Brachyury (T) (Figs 4A and B, and EV1A) compared to wild-type C57BL/6J littermates or wild-type CD1 embryos (Saykali *et al*,

© 2022 The Authors

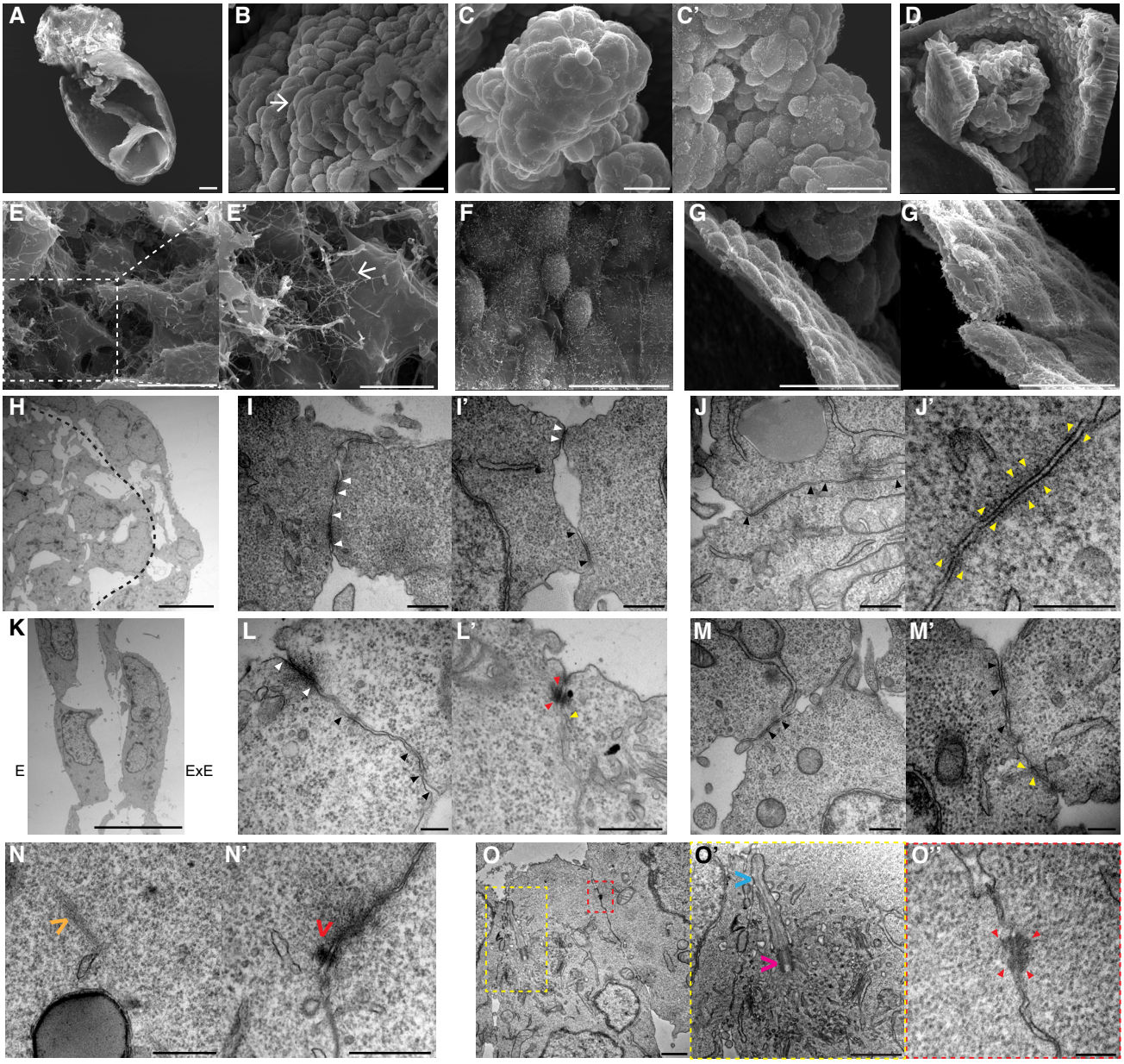


Figure 3. Electron microscopy of the ExE region at LB/NP stage.

A–G SEM images of an opened embryo (A), the ExE cavity wall (B) where blood islands are indicated by white arrow, the allantois surface (C, C′), an opened allantois (D) and its zooms (E, E′) where filaments are indicated by white arrows, the epiblast-derived side of the amnion (F), the mesoderm-derived side of the amnion (G) and its zoom (G′).

H–O TEM pictures in allantois (H–J), amnion (K–M), chorion (N) and allantois base (O). In H, allantois mesenchyme (Left) and cortex (Right) are separated by a black dashed line. (I, J) Junctions in internal (I, I′) and external (J, J′) allantois cells. In (K) the embryonic side of the amnion is on the left, and the ExE side on the right. (L, M) Junctions in the epiblast-derived side (L, L′) and the mesoderm-derived side (M, M′) of the amnion.

Data information: White (E, E′), yellow and red (O′–O″) dashed rectangles represent zoomed regions. Arrowheads point towards tight junctions (white), adherent junctions (black), desmosome-like junctions (red), and filaments (yellow). In chorion, the orange arrow indicates intermediate filaments (N) and the red arrow a desmosome (N′). In O′, axonem (cyan arrow) and basal body (magenta arrow) are annotated. Scale bars represent 100 μm (A, D), 50 μm (G), 25 μm (B, C, E, F), 20 μm (G′) 10 μm (H, K, P), 5 μm (E′), 1 μm (O, O′), 500 nm (I, J, L′, M, N), and 200 nm (J′, L, M′, O″).

2019). The distribution of the desmosomal protein Desmoglein 2 (Dsg2) was altered specifically in mesenchymal cells, where it was less sharply associated with the cell membrane compared to wild type (Figs 4B and EV1E). In contrast, Dsg2 pattern in epithelia, such as ExE ectoderm and visceral endoderm, was unchanged. The differentiation of mesoderm in endothelial progenitors appeared maintained as Pecam-1 expression was present in the chorion mesenchyme, blood islands, and allantois (Figs 4B and EV1E′).

© 2022 The Authors

To better characterize the consequence of keratin loss in late gastrulation embryos, we measured ExE structures (Fig 4C) in EB/NP *KtyII*$^{-/-}$ and their wild-type littermates. Values were normalized based on the length of the embryonic region, which was unaffected in mutants (Fig 4D). In *KtyII*$^{-/-}$ embryos, the exocoelomic cavity expansion was impaired (Fig 4E), the allantois was smaller (Fig 4F), and the amnion was shorter and thicker (Fig 4G and H). SEM of LB keratin-depleted embryos confirmed the restricted ExE cavity expansion (Fig 4I). Compared to wild-type littermates, allantois cortex in mutants was less smooth, with more convex apical cellular surfaces and deeper angles at cell–cell interface (Fig 4I′ and I″, and EV1F and F″). The phenotype of E7.5 embryos lacking keratin argues for a predominant function of KF in ExE mesenchymal tissues, in addition to epithelia.

Influence of the extracellular matrix on mesoderm cell behavior and cytoskeletal composition

Following up individual cells within the embryo was technically challenging; therefore, we turned to 2D culture of mesoderm explants dissected from the embryonic and ExE regions of E7.5 embryos. To record cell shape and speed, we used *Brachyury (T)*-Cre; *mTmG embryos (Saykali et al*, 2019), in which Cre-recombination in cells expressing Brachyury activates a membrane GFP reporter while non-recombined cells express membrane Tomato. Classically, mesoderm explants are plated on glass or plastic dishes coated with fibronectin (Fn1), an extracellular matrix protein produced by mesoderm cells which is abundant in basement membrane as well as in mesenchyme (Fig EV2A). Quantification from live imaging data showed that cells from both embryonic and ExE regions migrated at a speed almost twice higher than the one observed in *ex vivo* cultured embryos (Saykali *et al*, 2019) (Fig EV2B and C, Movie EV10). Similar observations were made on Matrigel or laminin, while explants plated on gelatin or collagen I failed to properly attach and expand. Collagen IV (ColIV) is also a component of the basement membrane and is present in ExE mesenchyme while being undetectable in embryonic mesoderm (Fig EV2A). Cells plated on a rigid substrate coated with collagen IV migrated at a speed of 0.6 μm/min, comparable to the one measured in embryos. To assess the influence of the matrix on keratin content, we performed a similar culture with explants from K8-eYFP embryos (Fig EV2B′). In these conditions, eYFP intensity was high on both coatings and did not vary according to the region of origin of the explants (Fig EV2D).

Since glass or plastic are several orders of magnitude harder than any biological tissue, we plated mesoderm cells on soft polyacrylamide gels with rigidity levels ranging from 5 to 20 kPa (Grevesse *et al*, 2013). On gels coated with Fn1, cells migrated at a speed close to that of embryonic mesoderm within the embryo, independent of the region of origin of the explant, with a trend toward increased speed on harder substrate and an optimal value reached on 15–20 kPa gels (Fig EV2E). Upon coating with ColIV, cell speed was closer to that of ExE mesoderm *ex vivo*, also independent of the region of origin and proportional to the gel rigidity, with a best match obtained on 10 kPa gels (Fig EV2F). Remarkably, K8-eYFP intensity content was lower on a soft substrate, compared to glass, for all conditions. The difference in K8-eYFP intensity between embryonic and ExE mesoderm cells was recapitulated only when cells were plated on gels coated with Fn1 (Fig EV2G).

Those experiments suggest that the keratin content of mesoderm cells is influenced by both the composition and the rigidity of the extracellular matrix and that cells from either region are capable to strengthen their KF network upon variation of the environment.

A common transcriptional signature for cytoskeleton and adhesion components in ExE mesenchyme enriched in KF

Specific qualitative and quantitative combinations of cytoskeletal proteins result in the unique viscoelastic characteristics of individual cells (Yoon & Leube, 2019). The mechanical properties of a tissue further depend on the type and abundance of cell–cell and cell–matrix junctions. To identify the expression patterns of cytoskeletal and adhesion molecules in epithelial and mesenchymal ExE cells and relate those to their respective KF abundance, we turned to scRNA-seq of sorted cells and micro-dissected tissues. An interactive atlas was created to facilitate usage of the clustered data (https://migeottelab.shinyapps.io/ExE_Atlas_Mouse_Gastrulation/). We previously performed bulk mRNA analysis of Mid/Late Streak (M/LS) stage mesoderm cells recovered from *T*-Cre; mTmG transgenic embryos (Fig 5A) (Saykali *et al*, 2019). Here, M/LS embryos from the same genetic background were manually cut at the embryonic-ExE boundary, GFP^{+} cells from each population were sorted by flow cytometry (Appendix Fig S2A), and single cells were sequenced. RNA velocity, which reveals the stream from immature to mature cell state (La Manno *et al*, 2018), assisted in cluster identification.

Embryonic mesoderm cells were relatively homogeneous, as expected at this stage of gastrulation. Based on gene expression and RNA velocity streams, we defined six clusters (Appendix Fig S2B and C). Five of those were adjacent: Primitive Streak, Nascent Mesoderm, Lateral Plate/Paraxial Mesoderm, Cranial/Heart Mesoderm, and ExE Mesoderm. A small independent cluster corresponded to Node precursors. Among the genes previously identified as enriched in embryonic mesoderm, single-cell analysis showed particularly interesting profiles for guidance molecules (Appendix Fig S2D). *Epha1* and *Ntn1*, for example, were found predominantly in the streak and node precursors, suggesting a role in transitions between epithelial and mesenchymal stages, while *EphA4* was expressed in Nascent and Paraxial/Lateral Mesoderm, but not in Anterior and ExE mesoderm, compatible with its later function in somitogenesis (Nieto *et al*, 1992). For ExE mesoderm cells, we distinguished three clusters (Appendix Fig S2E–G): Nascent Mesoderm, Endothelial/Erythroid Progenitors, and ExE mesenchyme. Apart from blood and vessels precursors, it was nonetheless difficult to predict cell fate based on expression profiles. Cells from different origins can indeed become undistinguishable once they acquire a similar fate, such as gut endoderm cells that may differentiate from definitive or visceral endoderm (Nowotschin *et al*, 2019). Localization in a particular region may also lead to harmonization of expression pattern, as illustrated by high K8 expression in all ExE germ layers.

To better understand cell differentiation trajectories, we characterized ExE populations at later stages and combined germ layer and spatial information. We manually isolated amnion, allantois, and chorion from *T*-Cre; mTmG embryos dissected at LB/NP stages (Fig 5B, 6A and 7A). All cells were sequenced to obtain a comprehensive atlas of each tissue. In addition to described expression profiles, each cluster was validated by immunostaining for at least one specific marker.

© 2022 The Authors

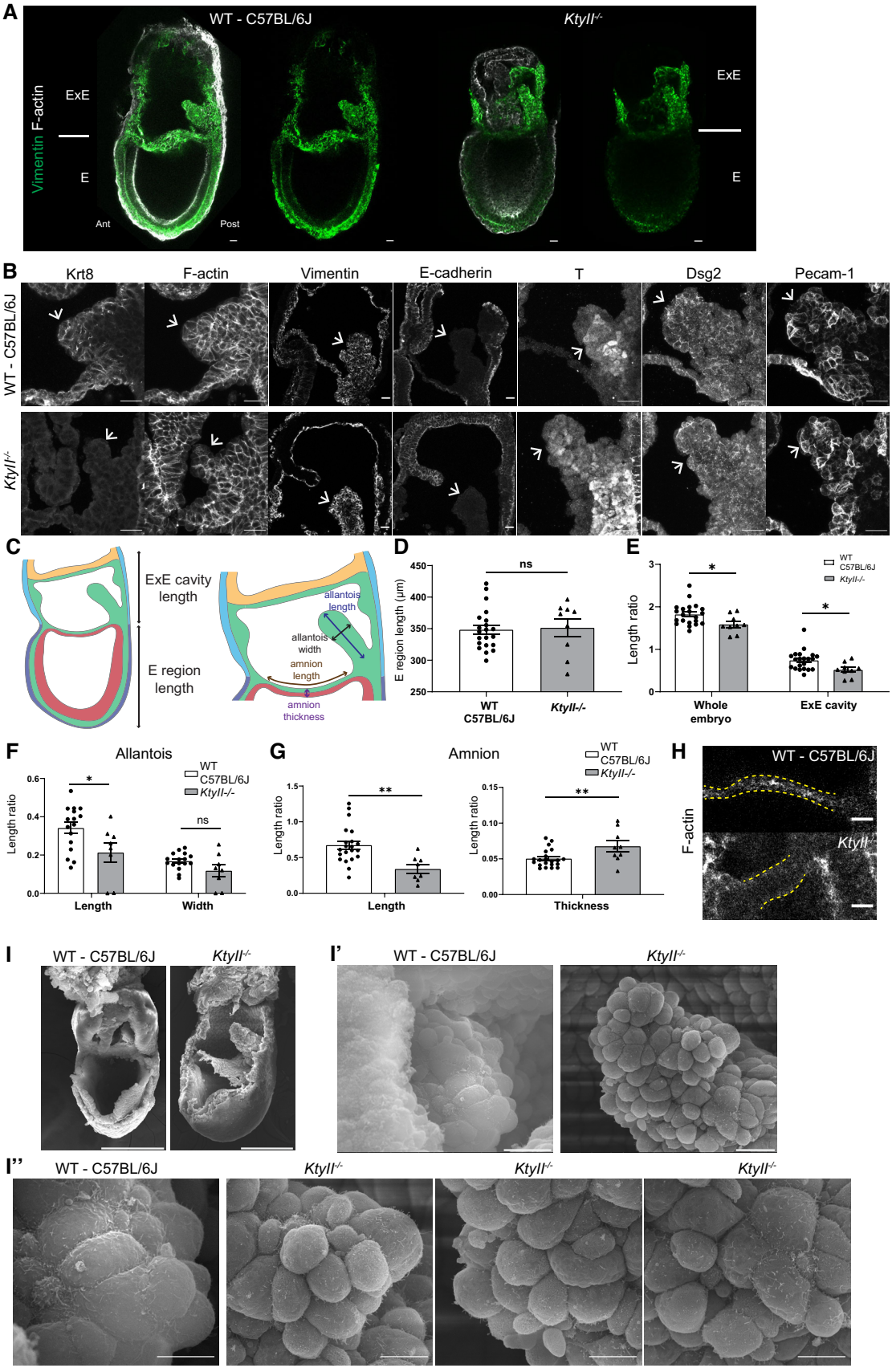


Figure 4.

© 2022 The Authors

Figure 4. Loss of keratin results in defective ExE region expansion.

A Z-projections of whole-mount C57BL/6J wild-type (WT, Left) and *KtyII*$^{-/-}$ (Right) embryos at LB stage stained for vimentin (green) and F-actin (Phalloidin, white). Scale bars represent 25 μm.

B Sagittal sections of C57BL/6J wild-type and *KtyII*$^{-/-}$ E7.5 embryos immunostained for Krt8 (n = 15 and n = 5, respectively), F-actin (n = 11 and 2), Vimentin (n = 5 and 1), E-cadherin (n = 1 and 1), T (n = 4 and 3), Dsg2 (n = 15 and 5) and Pecam-1 (n = 4 and 3). White arrows point toward allantois and scale bars represent 25 μm.

C Scheme for measurements.

D–G Quantification of embryo morphology at LB stage in C57BL/6J wild-type (white boxes/ black dots, n = 22 including 16 in which allantois could be measured), and *KtyII*$^{-/-}$ embryos (gray boxes/ black triangles, n = 9 including 8 in which allantois could be measured). (D) Embryonic region length. Ratios of whole embryo and ExE cavity lengths (E), allantois length and width (F) and amnion length and thickness (G), over embryonic region length. *P*-values were calculated using the Mann–Whitney-Wilcoxon test (ns: no statistical significance, *P < 0.05, **P < 0.005). Error bars represent SD.

H Z-projections of C57BL/6J wild-type (Top) and *KtyII*$^{-/-}$ (Bottom) embryos at LB stage stained for F-actin (Phalloidin, white). Amnion is delimited by yellow dashed lines. Scale bar represents 25 μm.

I, I″ SEM images of opened C57BL/6J wild-type (n = 3) and *KtyII*$^{-/-}$ (n = 2) LB stage embryos (I) with zooms on the allantois region (I′–I″). Scale bars represent 200 (I), 20 (I′), and 10 (I″) μm.

Source data are available online for this figure.

Amnion cells segregated in 5 clusters regrouped in two major populations (Figs 5C and EV3A). One had high *eGFP*, *Krt8*, and *Cdh2* and comprised Nascent Mesoderm (*Cdx2*, *Mesp1*) and Amnion Mesenchyme (*Acta2*, *Tagln*, *Col1a1*, *Dlk1*, *Nrp1*, *Vcan*). The low *eGFP* population represented Posterior Epiblast (*Cdh1*, *Fst*, *Ptn*) and Amnion Ectoderm (*Epcam*, *Cldn7*, *Krt8*, *Lrp2*, *Wnt6*; Figs 5D–F, and EV3B and C). Amnion also comprised a population of Erythroid Progenitors (*Lmo2*/*Runx1*) (Fig EV3D). A small ExE ectoderm cluster (*Elf5*, *Rhox5*) was likely formed by non-amnion cells that came along during dissection. Although *Krt8* was present in both epithelial and mesenchymal layers, immunostaining showed a distinct pattern for K8 in E-cadherin-positive epiblast-derived cells, where it appeared as apical dots, compared to mesoderm-derived cells where K8 was more abundant and formed filaments (Fig 5E). Cdx2 marked nascent mesoderm exiting the streak to become amnion mesoderm, with a posterior to anterior gradient (Fig 5G). Amnion mesoderm showed high expression of Col1a1 and Nrp1, also present in exocoelomic cavity walls and chorion mesenchyme (Figs 5H and EV3B). Amnion ectoderm, compared to epiblast, had similar Epcam, lower E-cadherin and Claudin7, and higher K8 (Figs 5E, F and I, and EV3C). Specific markers included *Wnt6* and *Lrp2* (Fig 5F). Immunostaining for Lrp2 showed a punctate pattern in amnion ectoderm (Figs 5I and EV3C), compatible with its function in endocytosis. In *KtyII*$^{-/-}$ embryos, the layer identity was maintained, as illustrated by immunostaining for the mesenchyme marker Nrp-1 (Fig 5J) and the ectoderm marker Lrp2 (Fig 5K).

In chorion, we defined 5 clusters (Figs 6B–D, and EV4A): Chorion Ectoderm/Labyrinth Progenitors, Trophoblast Progenitors, Proximal Chorion Ectoderm, Blood Islands, and Chorion Mesenchyme. *eGFP*$^{+}$ cells formed a discrete *Cdh2*-positive mesenchymal cluster, and additional cells were scattered among the *Cdh1*-positive population, compatible with *Brachyury* expression in ExE ectoderm (Inman & Downs, 2006) (Fig 6C). *Krt8* was present in both epithelial and mesenchymal cells (Fig 6C). *Cdx2* and *Elf5* were present in most cells, except mesenchyme and blood islands (Figs 6D and E, and EV4B). RNA Velocity (Figs 6B and EV4A) showed streams within each population as well as one from trophoblast progenitors (Sox2 (Figs 6D and F, and EV4B), *Eomes*) toward chorion ectoderm (*Rhox6* (Chun *et al*, 1999), Gata2 (Fig 6D and F)). Sox2 and Gata2 showed very little overlap. Proximal chorion displayed a gene profile resembling that of ectoplacental cone (*Ascl2*, an imprinted gene expressed in trophectoderm then mostly restricted to ectoplacental cone [Fig 6D] (Guillemot *et al*, 1994)). Cebpb (Simmons *et al*, 2008) was present in the three epithelial populations, enriched in proximal ectoderm (Fig 6D and G). A subpopulation of cells, representing labyrinth progenitors, already expressed *Gcm1*, later found on the tip of villi in the chorion-derived component of labyrinth (Simmons *et al*, 2008) (Fig EV4C). *Dlx3* (Fig EV4C) is predominantly detected in ectoplacental cone (Simmons *et al*, 2008) and is required for labyrinth morphogenesis (Morasso *et al*, 1999). *Dlx3* and *Gcm1* were essentially mutually exclusive (Fig EV4C), consistent with Dlx3 inhibition of *Gcm1* transcriptional activity (Li & Roberson, 2017). *Gcm1*$^{+}$ cells already had a distinctive transcriptomic profile at that early stage (Fig EV4C). Mesoderm-derived cells (*Fn1*) were subdivided according to their prospective endothelial (*Dlk1*, *Acta2*) or erythroid (*Hbb-bh1*) identities (Figs 6D and H, and EV4D). The pattern and level of Dlk1 and Acta2 were maintained in chorion mesenchyme of keratin-depleted embryos (Fig 6I). Imprinted genes were found in all chorion populations independent of their germ layer of origin. There were also multiple genes involved in transmembrane transport (*Slc38a4* (Matoba *et al*, 2019)), endocytosis (*Vamp8*) and metal metabolism (*Mt1*, *Mt2*, *Fthl17a*), reflecting chorion's prospective role in embryo nutrition.

Allantois, as expected, was essentially composed of mesenchymal (*eGFP*, *Cdh2*) cells with high *Krt8* expression (Figs 7B and C, and EV5A). Based on known gene expression profiles and RNA velocity streams, 6 clusters were individualized (Fig 7B and D): Primitive Streak (T [Figs 7E and EV5B] (Inman & Downs, 2006)), *Fgf8*, Allantois Base (*Cdx4*, T, Ifitm3 [Fig 7E and F]), Allantois Cortex (*Krt8* and *18*, Stard8, Cdh11, Nrp1 [Figs 7G and EV5C]), Allantois Mesenchyme (*Tbx4*, *Vcan*, Pitx1 [Figs 7H and EV5D]), Endothelial Progenitors (*Tal1*, *Hhex*, Kdr [Figs 7I and EV5E]), and Erythroid Progenitors (Runx1 [Fig 7J], *Lmo2*). Using a polygenic score, we defined a small subpopulation of Primordial Germ Cells (PGC) within the Primitive Streak cluster (Fig EV5F), providing a snapshot of the PGC expression profile while in the allantois and highlighting the need to combine multiple markers, as none appeared PGC-specific. Allantois mesenchyme had high *Versican (Vcan)* expression, compatible with the importance of proteoglycans in protecting blood vessels in the umbilical cord (Nandadasa *et al*, 2020). Vasculogenesis has been described to start at the distal end of the allantois and to progress proximally (Inman & Downs, 2006). We were able to identify early expression profiles of specific endothelial populations, such as potential artery progenitors expressing

© 2022 The Authors

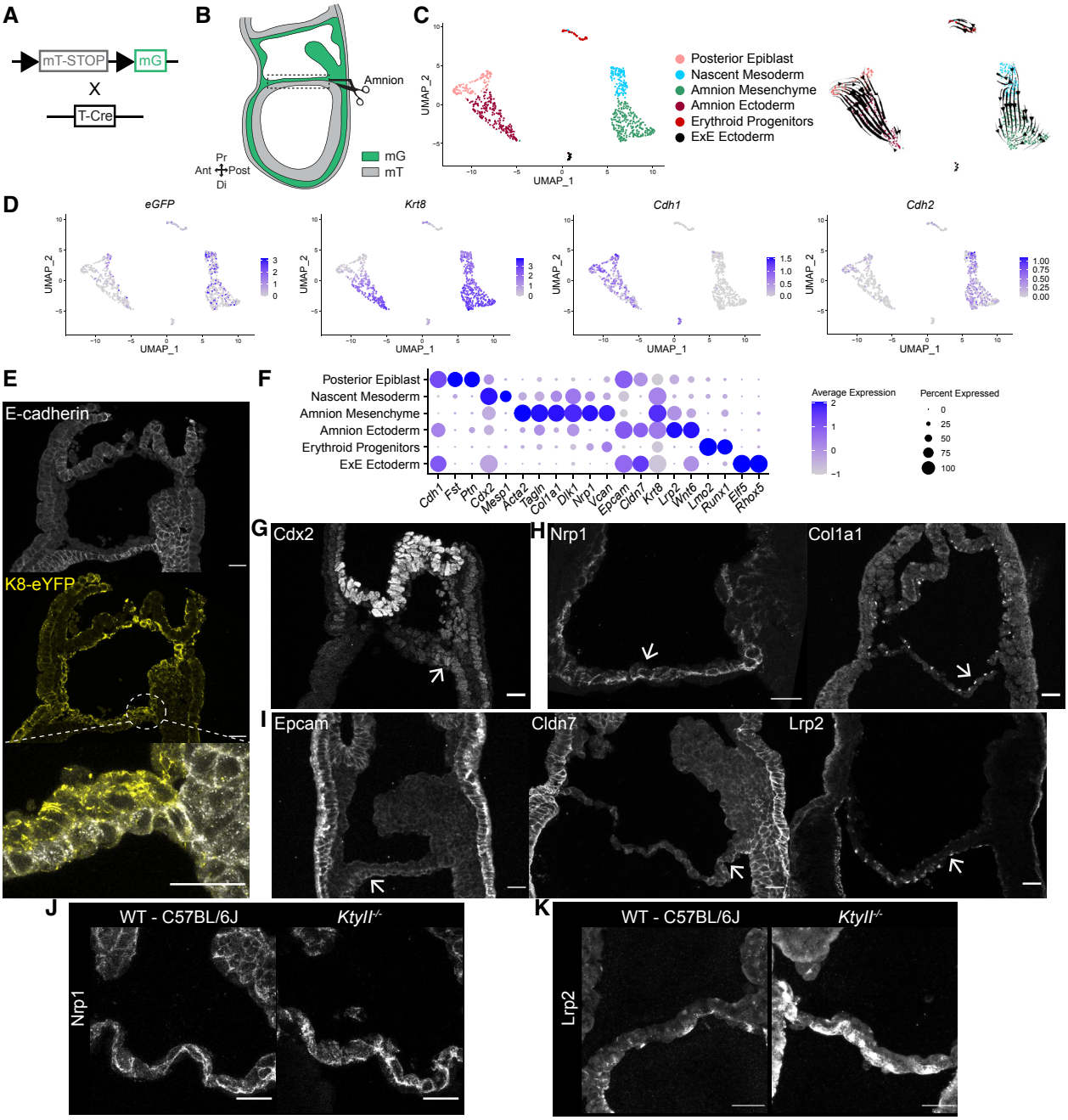


Figure 5. Amnion single-cell transcriptome.

A In *Brachyury (T)*-Cre; mTmG embryos, mesoderm-derived cells express membrane eGFP (mG, green) and the other cells membrane tdTomato (mT, gray).

B Scheme of amnion isolation.

C Uniform Manifold Approximation and Projection (UMAP) (Left, color-coded) and RNA velocity (Right, black arrows show streaming directions from unspliced to spliced RNA) of amnion cells where 6 unsupervised clusters were identified.

D UMAP of *eGFP*, *Krt8*, *Cdh1*, and *Cdh2*.

E EB K8-eYFP embryo stained for eYFP (yellow) and E-cadherin (white) (n = 7) (Top). Dashed white area zoom on an amnion region which highlights the two cell layers (Bottom).

F Dot plot of specific gene expression in amnion clusters.

G Immunostaining for Cdx2 (n = 20).

H Immunostaining for Nrp1 (n = 8) and Col1a1 (n = 7), primarily expressed in Amnion Mesenchyme.

I Immunostaining for Epcam (n = 12), Cldn7 (n = 7), and Lrp2 (n = 6), primarily expressed in Amnion Ectoderm.

J–K Sections of C57BL/6J wild-type and *Ktyll*$^{-/-}$ E7.5 embryos immunostained for Nrp1 (K) (n = 8 and 2, respectively), and Lrp2 (L) (n = 3 and 2).

Data information: White arrows point toward signal in amnion. In (E) and (G–L), sagittal sections with anterior to the left. Scale bars represent 25 μm.
Source data are available online for this figure.

© 2022 The Authors

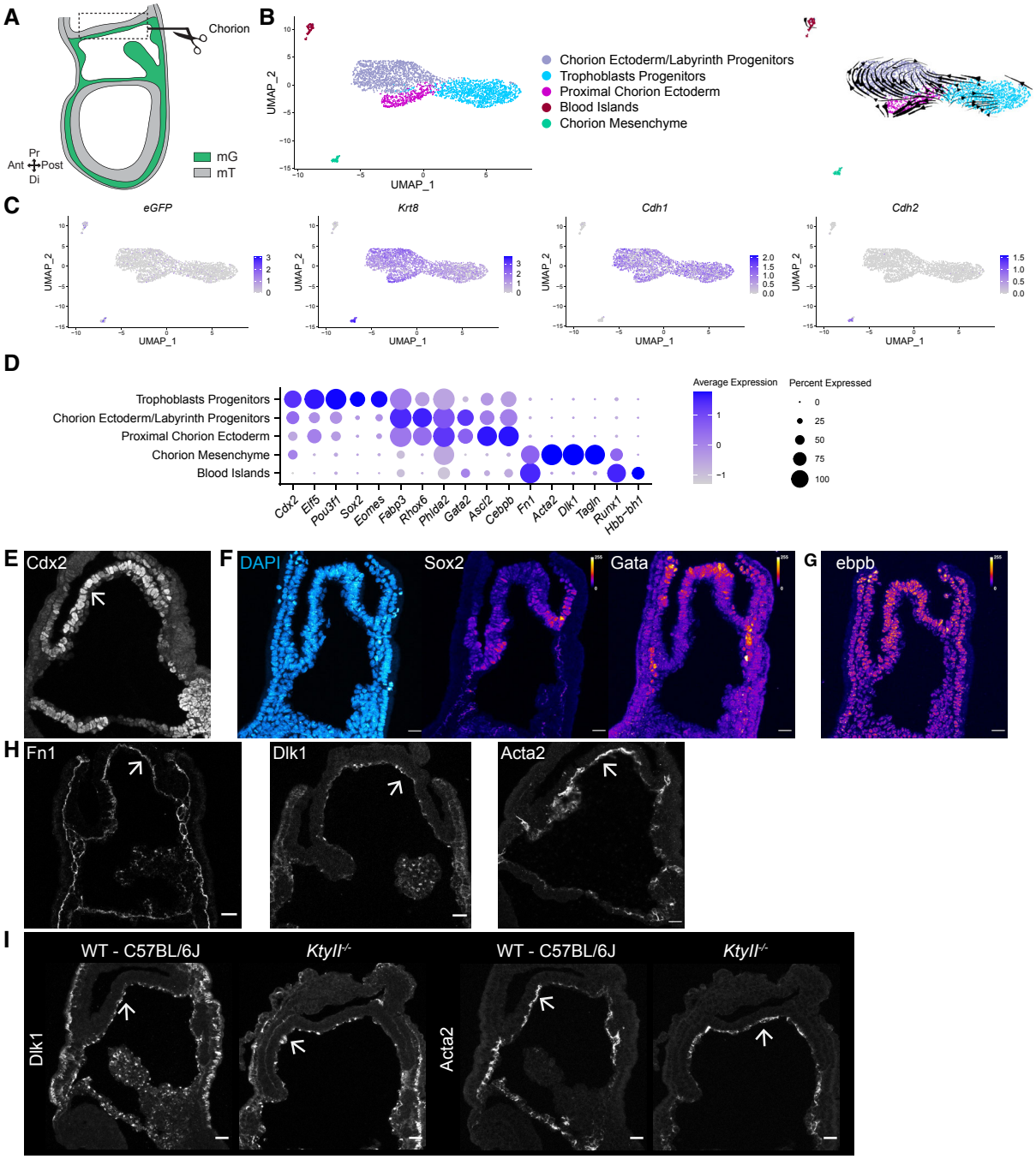


Figure 6. Chorion single-cell transcriptome.

A Scheme of chorion isolation where mesoderm is in green (mG), and the other cells are in gray (mT).
B UMAP (Left) and RNA velocity (Right) of chorion cells where 5 unsupervised clusters were identified.
C UMAP of *eGFP*, *Krt8*, *Cdh1*, and *Cdh2*.
D Dot plot of specific gene expression in chorion clusters.
E Immunostaining for Cdx2 (n = 20).
F Immunostaining for DAPI (cyan, left), Sox2 (middle), and Gata2 (right). Sox2 is primarily expressed in Trophoblast Progenitors and Gata2 in Chorion Ectoderm.
G Immunostaining for Cebpb, detectable in most cells with variable intensity.
H Immunostaining for Fn1 (n = 22), Dlk1 (n = 8), and Acta2 (n = 12), primarily expressed in Chorion Mesenchyme.
I Sections from C57BL/6J wild-type and *Ktyll*$^{-/-}$ LB embryos immunostained for Dlk-1 (n = 8 and 4, respectively) and Acta2 (n = 6 and 3).

Data information: (F) and (G) are adjacent sections from the same embryo (n = 4). White arrows point toward the signal in chorion. Sagittal sections with anterior to the left. Scale bars represent 25 μm.
Source data are available online for this figure.

© 2022 The Authors

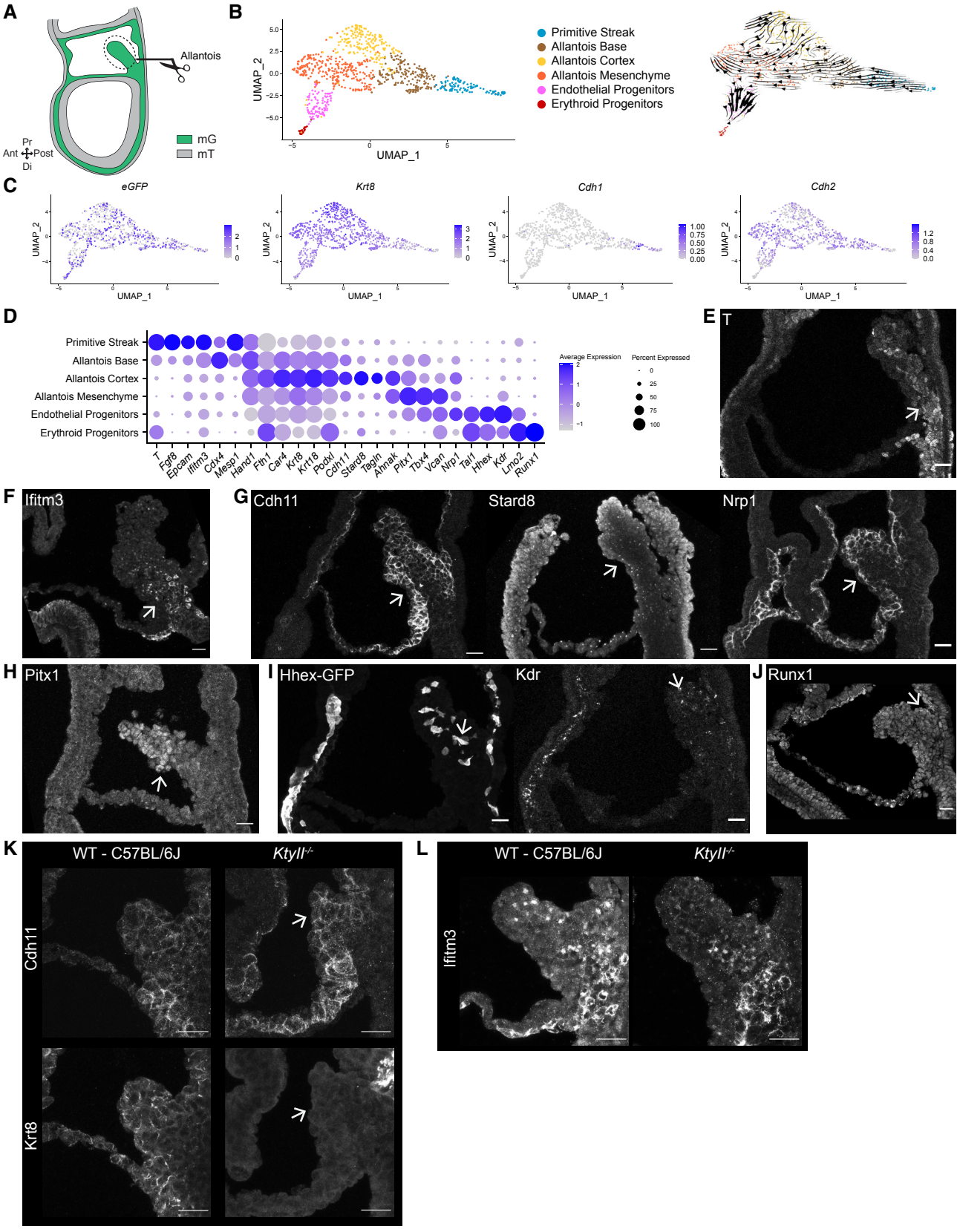


Figure 7.

© 2022 The Authors

Figure 7. Allantois single-cell transcriptome.

A Scheme of allantois isolation where mesoderm is in green (mG), and the other cells are in gray (mT).
B UMAP (Left) and RNA velocity (Right) of allantois cells where 6 unsupervised clusters were identified.
C UMAP of *eGFP*, *Krt8*, *Cdh1*, and *Cdh2*.
D Dot plot of specific gene expression in allantois clusters.
E Immunostaining for T ($n = 5$) (Primitive Streak and Allantois Base).
F Immunostaining for Ifitm3 ($n = 7$) (Allantois Base).
G Immunostaining for Cdh11 ($n = 9$), Stard8 ($n = 4$) and Nrp1 ($n = 8$) (Allantois Cortex).
H Immunostaining for Pitx1 ($n = 4$) (Allantois Mesenchyme).
I *Hhex*-GFP ($n = 5$) and immunostaining for Kdr ($n = 8$) (Endothelial Progenitors).
J Immunostaining for Runx1 ($n = 3$) (Erythroid Progenitors).
K, L Sections from C57BL/6J wild-type and *Ktyll*$^{-/-}$ LB embryos immunostained for Cdh11 (Top) and Krt8 (Bottom) (K, $n = 8$ and 4, respectively) and Ifitm3 (L, $n = 2$ and 2).

Data information: White arrows point toward signal in allantois. Sagittal sections with anterior to the left. Scale bars represent 25 μm.

Source data are available online for this figure.

Dll4 (Arora & Papaioannou, 2012) (Fig EV5G). Like amnion and chorion mesoderm, allantois cortex expressed *Acta2* and *Tagln*. It was also enriched for transcripts of genes associated with apical identity, such as *Podxl*, endosomal transport (*Stard8*, also called *Dlc3* (Noll *et al*, 2019)), as well as transmembrane transport of nutrients (*Scl2a1*), ions (*Fth1*) and gases (*Car4*), suggesting that outer allantois cells start acquiring functions that will be essential for the functionality of the labyrinth even prior to attachment to the chorion. Although KF in allantois cortex appeared continuous across several cells, we could not visualize mature desmosomes by electron microscopy; scRNA-seq detected desmosome components (such as *Dsg2*, *Dsp*, *Dsc2*, or *Pkp4*) in allantois cells, without cluster specificity. Compatible with TEM data, tight junction constituents *Cldn12*, *Tjp1* and *2* were present in cells from multiple clusters. Among cadherins, Cdh11 stood out as being more abundant in external allantois cells, where it co-localized with Krt8 at cell–cell contacts (Fig 7G and K). In allantois mesenchyme, Krt8 was perinuclear and Cdh11 was less abundant. In keratin-depleted embryos, Cdh11 level was maintained (Fig 7K) although its expression pattern appeared less contrasted between cortex and mesenchyme in the most affected mutants. The allantois architecture was preserved, as illustrated by the distribution of Ifitm3 (Fig 7L).

Discussion

Krt intermediate filaments have a higher elasticity than actin and microtubules filaments; they can stretch several times their initial length before reaching the yield point (Sanghvi-Shah & Weber, 2017). They play a major role in cell resistance to external mechanical stress, as illustrated by the lower elasticity and higher deformability of keratinocytes lacking keratin (Ramms *et al*, 2013; Seltmann *et al*, 2013). Here, live imaging of mouse embryos with a knock-in K8-eYFP fusion allele identified KF containing cables in all tissues facing the exocoelomic cavity (yolk sac, amnion and chorion mesenchyme, allantois cortex), reminding of the supracellular actomyosin network described in wound healing (Martin & Lewis, 1992), *Drosophila* germ band expansion (Fernandez-Gonzalez *et al*, 2009), and mouse embryo neural tube closure (Galea *et al*, 2017). Interestingly, epithelial cells subjected to extreme stretch *in vitro* reorganize their cytoskeleton such that keratin 18 filaments form connections between cells (Latorre *et al*, 2018). Culture of mesoderm explants on substrates of various rigidity and composition pointed towards a role of the physical environment in regulating the KF network. Similarly, the kinetics of the keratin turnover cycle (Pora *et al*, 2020) and the alignment and interconnection of keratin bundles (Laly *et al*, 2021) are modulated by the stiffness of the substrate in keratinocytes. Embryos devoid of keratin had a small exocoelomic cavity, a short and thick amnion, as well as defective allantois elongation. Allantois cortex was less regular, as lateral cell borders met at sharper angles in mutant embryos. We previously showed that ExE mesoderm had a lower content in actin filaments than embryonic mesoderm in E7.25 embryos. At later stages, we did not detect supracellular F-actin cables around the exocoelomic cavity or at amnion borders. Altogether, these observations suggest that the KF network may play a prominent role in bridging cells and harmonizing tension during ExE membranes formation and expansion. Similarly, human fetal mesenchyme and amniotic epithelium co-express keratin and vimentin (Khong *et al*, 1986; Beham *et al*, 1988). Cytoskeletal networks in amniochorion participate to fetal membranes' capacity to withstand increase in intrauterine pressure during contractions, and recover from mechanical trauma such as amniocentesis (Ockleford *et al*, 1993).

Smooth muscle alpha-2 actin (*Acta2*), transgelin (*Tagln*, also called *SM22alpha*), and cadherin-11 were co-expressed with *Krt8* in amnion and chorion mesenchyme as well as in allantois cortex. *Acta2*, *Tagln* and *Cdh11* are TGFβ-inducible genes, compatible with high BMP signaling in the ExE region. Acta2 is a marker for myofibroblasts and smooth muscle cells. It plays an essential role in vascular contractility, and *ACTA2* mutations in human cause a variety of vascular diseases (Guo *et al*, 2007). Acta2 expression is unaltered in keratin-depleted embryos, in which it may partly compensate for the loss of KF. Transgelin binds directly to actin filaments and was shown *in vitro* to cause actin gelation due to conversion of loose filaments into a tangle meshwork (Shapland *et al*, 1993). Cadherin-11 is a type II classical cadherin predominantly expressed in mesenchymal tissues (Hoffmann & Balling, 1995). During embryonic development, it is required for neural crest survival and migration (Manohar *et al*, 2020). Its expression in fibroblasts is correlated with mechanical stress; switching from cadherin-2 to 11 is associated with transition from low contractile migratory fibroblast to highly contractile myofibroblast (Pittet *et al*, 2008). In frog mesendoderm, local forces applied to C-cadherin result in recruitment of KF to cadherin complexes via plakoglobin

© 2022 The Authors

(Weber *et al*, 2012). K8 and cadherin-11 co-localize at cell-cell junctions in allantois cortex. It is therefore conceivable that KF and cadherin-11 might interact at sites of higher tension. Single-cell transcriptome of MS/LS ExE mesoderm cells revealed that *Acta2*, *Tagln* and *Cdh11* were already detectable at lower levels. Collectively, this suggests that mesenchymal cells lining the exocoelomic cavity have a common differentiation program which may help accommodate rapid morphology changes.

A series of scRNA-seq studies have offered detailed reference atlases (Nowotschin *et al*, 2019; Pijuan-Sala *et al*, 2019; Marsh & Blelloch, 2020). The mouse gastrulation single-cell atlas currently lacks some ExE tissues (Pijuan-Sala *et al*, 2019). Furthermore, identification of cell location is based solely on gene expression and can thus be confounded by similarity in transcription profiles. An RNA sequencing study of single nuclei from E9.5 to E14.5 mouse embryo placenta resolved all populations of the mature labyrinth, including fetal mesenchyme clusters characterized by *Acta2* expression (Marsh & Blelloch, 2020). Here we provide an additional database that includes spatial and germ layer information for early ExE structures that had not been previously individualized due to absence of specific markers. Through scRNA-seq of micro-dissected amnion, we found a series of genes differentially expressed between epiblast and amnion ectoderm, including *Krt8*, *Lrp2* and *Wnt6*. *Wnt6* is a conserved amnion ectoderm marker in mouse (Parr *et al*, 2001), non-human primate (Yang *et al*, 2021), and human (Tyser *et al*, 2021) embryos. *WNT6* and *LRP2* were co-expressed in a subset of human embryo ectoderm cells (Tyser *et al*, 2021), similar to what we observed in amnion epithelium. As Wnt6 has been shown to regulate epithelial-mesenchymal transition in other contexts (Schmidt *et al*, 2004; Krawetz & Kelly, 2008), it may be compatible with an intermediate state favorable for the rapid expansion of amnion upon embryo turning.

Mouse embryo lethality around mid-gestation is almost always associated with severe placental defects (Rossant & Cross, 2001; Perez-Garcia *et al*, 2018). For a proportion of those genes, epiblast-specific mutants identified the germ layer responsible for lethality. *Bap1* phenotype, for example, was partially rescued by wild-type trophectoderm; interrogating our atlas showed *Bap1* expression in chorion and allantois. The *Crb2* phenotype however was not rescued in epiblast-specific mutants, compatible with its specific transcription in allantois. A number of mouse mutants have been shown to display defective chorio-allantoic union (Watson & Cross, 2005; Inman & Downs, 2007), notably through deletion of *Vcam-1* (expressed in allantois (Gurtner *et al*, 1995)) or its partner alpha 4 integrin (*Itga4*, expressed in chorion mesoderm (Yang *et al*, 1995)). Most described mutants have incomplete penetrance, suggesting there might be functional redundancy. Based on single-cell profiles in allantois and chorion, we interrogated CellPhone DB (Efremova *et al*, 2020) to look for ligand-receptor couples that could play a role in allantois directional growth towards chorion. To increase specificity, we focused on allantois cortex and mesenchyme versus chorion mesoderm and ectoderm (Fig EV5H). Significant interactions included previously described actors of chorio-allantoic fusion such as BMP2, 4, 5 and 7, FGFR2, or Wnt7b (Watson & Cross, 2005; Inman & Downs, 2007) as well as an array of potential new targets either within the BMP, FGF and Wnt pathways or belonging to other pathways, such as Neuropilin, Ephrin, and Notch.

Although the human embryo displays a different geometry at that stage, cell populations involved in formation of amnion, placenta, and umbilical cord are conserved and likely to rely on similar molecular modules. Single-cell analyses of first trimester placentas identified placental and decidual cell types at the maternal-fetal interface. Fibroblasts of both maternal (Vento-Tormo *et al*, 2018) and fetal (Suryawanshi *et al*, 2018) origins had high ACTA2 and TAGLN. Fetal fibroblasts were the primary source of DLK1 (Suryawanshi *et al*, 2018), similar to mouse in which Dlk1 is abundant in ExE mesoderm as well as allantois and amnion mesenchyme. Time and space resolved atlases of mouse embryo and placenta are precious tools to guide interpretation of data from rare human samples.

Here we captured cytoskeleton, cell, and tissue organization during formation of mouse embryo support organs, uncovered a major role for keratin intermediate filaments in expansion of ExE tissues, and provided a regional single-cell transcriptome for mesoderm, amnion, chorion, and allantois. High time and space resolution imaging of K8-eYFP embryos bearing fluorescent markers for nuclei and cytoskeletal components would be very valuable to better comprehend KF interplay with actomyosin and microtubules. To decipher the role of KF in ExE mesenchyme at the molecular and physical level, explanted mesoderm cells from wild-type and keratin-depleted embryos could be challenged by varying the composition and rigidity of the substrate, applying stretch (Latorre *et al*, 2018), or knocking down potential partners within adhesion complexes. Similar studies could be undertaken on appropriate mouse and human stem cells-derived germ layer and embryo models to help explore essential steps in the establishment of ExE membranes in human.

Materials and Methods

Mouse breeding and embryo collection

Mouse colonies were maintained in a certified animal facility in accordance with European guidelines. Experiments were approved by the local ethics committee (CEBEA). Mouse genomic DNA was isolated from ear biopsies treated for 1 h at 95°C in NaOH to simultaneously genotype and identify animals. Mouse lines were K8-eYFP (Schwarz *et al*, 2015), mTmG (Muzumdar *et al*, 2007) (Jackson laboratory), *Brachyury (T)*-Cre *(Feller et al*, 2008), *Hex*-GFP (Srinivas *et al*, 2004), all bred on a CD1 background, and *KrtyII*$^{+/-}$ (Vijayaraj *et al*, 2009), bred on a C57BL/6J background. Embryos were recovered at the appropriate time point after observation of a vaginal plug at day 0. Embryos were dissected in Dulbecco's modified Eagle medium (DMEM) F-12 (Gibco) supplemented with 10% Fetal Bovine Serum (FBS), 1% Penicillin/Streptomycin (P/S) and L-glutamine, and 15 mM HEPES, using #5 forceps and tungsten needles under a transmitted light stereomicroscope. Bright-field pictures of the litter or single embryo were taken before any other manipulation to ensure adequate staging. Genotyping of mutant embryos was performed after a lysis step (Lysis Buffer [Viagen]) with 1.5% Proteinase K (Qiagen).

Isolation of mesoderm explants

LB embryos were pooled and incubated at 4°C in pancreatic enzymes/trypsin solution (2.5% of pancreatin from porcine

 © 2022 The Authors

pancreas (Sigma, P1750) + 0.5% trypsin (Thermo Fisher, 15090046) in PBS) for 18min then washed in DMEM supplemented with 10% FBS and 1% P/S. E and ExE mesoderm layers were manually isolated using finely sharpened forceps and tungsten needles. Isolated explants were transferred into dishes with specific substrates (rigidity and coating) filled with DMEM supplemented with 10% FBS and 1% P/S. Explants were incubated at 37°C during 2–4 h before imaging.

Gel preparation

As reported previously (Bruyère *et al*, 2019), hydroxy-polyacrylamide (hydroxy-PAAm) hydrogels of 1–50 kPa in Young's modulus were fabricated by mixing acrylamide (AAm, A8887, Sigma), bisacrylamide (bis-AAm, 146072, Sigma) and *N*-hydroxyethylacrylamide (HEA, 697931, Sigma) monomers (19, 20, 58). The polymerization was initiated with ammonium persulfate (APS) and *N*, *N*, *N*′, *N*′-Tetramethylethylenediamine (TEMED) and the hydrogel stiffness was characterized in indentation mode by microindentation (Chiaro, Optics11). After three washes in sterile water, hydrogels were ready for coating.

Surface coating

For glass coating, solutions of fibronectin (F1141, Sigma) at 75 μg/ml and collagen IV (354233, Corning) at 100 μg/ml were incubated for at least 1 h at 4°C before washing with distilled water. For gel coating, a droplet of 200 μl of 75 μg/ml of fibronectin or collagen IV was added under sterile conditions. Coating was considered complete when the droplet dried (2–4 h). The gel was rehydrated with distilled water and stored at 4°C.

scRNA-seq sample preparation

T-Cre; mTmG embryos were collected from multiple pregnant females at E7.5, and embryos at the appropriate stage were pooled. Embryonic and ExE portions were separated by manually cutting the embryo with finely sharpened forceps. For embryonic and ExE mesoderm cells samples, MS/LS embryos were digested in dissociation buffer (1% 100 mM EDTA + 4% of 2.5% trypsin in Phosphate Buffer saline [PBS]), and the two pure GFP positive populations were sorted through flow cytometry (FACSARIA III, BD), directly in DMEM F-12 supplemented with 10% FBS and 15 mM HEPES. For ExE structures samples, LB embryos were pooled and incubated at 4°C in pancreatic enzymes/trypsin solution (2.5% of pancreatin from porcine pancreas [Sigma, P1750] + 0.5% trypsin [Thermo Fisher, 15090046] in PBS) for 18min then washed in DMEM supplemented with 10% FBS and 1% penicillin-streptomycin. For ExE structures, allantois, amnion, and chorion were manually dissected in PBS supplemented with 0.04% BSA with finely sharpened forceps and tungsten needles. ExE structures were then incubated at 37°C in accutase (Sigma, A6964)/0.25% trypsin (Gibco, 1509-046) for 20 min (with gentle agitation at 10 min). 30% DMEM/F-12 with HEPES, 20% FBS, and 50% 4 mM EDTA were added to the mix. Clumps were triturated by mouth pipetting and the solution was filtered in a non-binding RNA-free microfuge tube (Ambion) with Flow MI cell 40 μm to remove debris. The solution was centrifuged at 450 *g* for 4 min. Cells were resuspended in 50 μl in FHM (Merck, MR-024-D). For both approaches, cells were checked for viability and counted using a hemocytometer.

scRNA-seq analysis

Single-cell transcriptomics was performed with the Chromium Single Cell microfluidic device (10X Genomics). Loaded cells were individually barcoded with a 10X Chromium controller according to the manufacturer's recommendations. The libraries were prepared using the Chromium Single Cell 3′ Library Kit (V3-chemistry, 10X Genomics), and sequenced on NovaSeq 6000 (Illumina) sequencing platform. Each sample sequenced was obtained from one experiment except for amnion that is a combination of two samples sequenced separately. 2,742 and 1,159 cells were sequenced for embryonic and ExE GFP positive cells, respectively, with a mean number of 24,619 and 56,514 reads per cell and 3,294 and 4,505 genes per cell. For the two amnion samples, 314 and 503 cells were sequenced, with a mean number of 214,164 and 133,664 reads per cell and 5,956 and 5,173 genes per cell. 3,732 and 912 cells were sequenced for chorion and allantois, respectively, with a mean number of 25,613 and 70,891 reads per cell and 3,065 and 4,747 genes per cell.

Sequencing reads were aligned and annotated with the mm10 reference dataset provided by 10X Genomics. *Cre*, *eGFP*, and *tdTomato* sequences were added by following 10X Genomics instructions. Sequencing reads were demultiplexed using CellRanger (version 3.0.2) with default parameters. Number of genes, total counts of UMI, and the percentage of mitochondrial genes were utilized for quality control. Expression value scaling and normalization, PCA and UMAP dimensionality reductions and clustering were performed using the Seurat R package (version 3.0.1) (Butler *et al*, 2018). Clusters were defined using Seurat at multiple resolutions (0.2, 0.3, 0.5) and marker gene discovery was performed using the FindAllMarkers function of the Seurat package using the Wilcoxon Ranked Sum test. Markers were then selected by setting the threshold to all genes with an adjusted *P*-value lower than 0.25. Two output graphs were generated: UMAP and Dot plot. On UMAP, each point represents a cell, and its position is based on the cell embedding determined by the PCA. Color depends on the cluster attribution. On Dot plot, the size of the dot encodes the percentage of cells expressing the gene within a cluster and the color encodes the average expression level across all cells within the cluster. Blue means high expression and gray means low expression. RNA velocity was performed on dataset processed with Seurat as previously described. Velocyto (La Manno *et al*, 2018) and scvelo (Bergen *et al*, 2020) packages were run on Python 3 by following the described on-line pipelines. The stochastic model was used for the RNA velocity models based on the balance of unspliced and spliced mRNA levels and their covariation. Receptor-ligand interaction analysis was performed utilizing CellPhoneDB package (Efremova *et al*, 2020). As outlined in CellPhoneDB guidelines, the input data was prepared after extracting from Seurat object. Mouse gene names were converted to orthologues of human gene names which were retrieved from BioMart (Smedley *et al*, 2009). The statistical method was run using the default parameters (10% threshold). Dot plot was plotted using the entire list of significant interaction pairs in the following comparisons: allantois cortex vs. chorion mesoderm, allantois mesenchyme vs. chorion mesoderm, allantois cortex vs. chorion ectoderm and allantois mesenchyme vs. chorion ectoderm.

© 2022 The Authors

For a detailed description of the terms, please refer to the documentation of CellPhoneDB package.

Whole-mount and section immunostaining

For immunofluorescence, embryos were fixed in PBS containing 4% paraformaldehyde for 2 h at 4°C. For sagittal sections, fixed embryos were cryopreserved in 30% sucrose, embedded in OCT, and cryosectioned at 7–10 μm. Staining was performed in PBS containing 0.5% Triton X-100, 0.1% BSA, and 5% heat-inactivated horse serum. Primary antibodies were incubated overnight, and secondary antibodies were incubated for 2 h at RT. Sections and whole-mount embryos were imaged on a Zeiss LSM 780 microscope equipped with Plan Apochromat 20×/0.8 M27 and an LD C Apochromat 40×/1.1 W Korr M27 objectives with 1, 3, or 5 μm Z-intervals. Image processing was done on ImageJ, Icy, or Arivis.

Antibodies

The following primary antibodies were used: anti-Acta2 (rabbit, 1:100, Cell Signaling, 19245T), anti-Cdh1 (rabbit, 1:500, Cell Signaling, 877-616), anti-Cdh11 (rabbit, 1:200, Cell Signaling, 442S, Lot 1), anti-Cdx2 (rabbit, 1:200 Abcam, ab76541), anti-Cebpb (rabbit, 1:250, Novus, NBP2-57075), anti-Cldn7 (rabbit, 1:50, Thermo Fisher, 34-9100), anti-Col1a1 (rabbit, 1:50, Thermo Fisher, PA1-85319), anti-ColIV (goat, 1:500, EMB Mllipore Corp, AB769), anti-Dlk1 (rat, 1:250, MBL, D187-3), anti-Dsg2 (rabbit, 1:250, gift from Leube's lab (Schlegel *et al*, 2010), anti-Epcam (rat, 1:100, Biolegende, 1182020), anti-Fn1 (rabbit, 1:1,500, Sigma, F3648), anti-Ifitm3 (rabbit, 1:50, Abcam, ab15592), anti-Gata2 (rabbit, 1:500, Invitrogen, PA1100), anti-GFP (goat, 1:500, Abcam, ab6673), anti-GFP (rabbit, 1:500, Life technology, A11122), anti-Kdr (rabbit, 1:100, Cell Signaling, 55B11), anti-Krt8 (rat, 1:100, TROMA-I-S, DSHB, AB_531826), anti-Lrp2 (rabbit, 1:50, Abcam, ab76969), anti-Nrp1 (goat, 1:50, R&D, AF566-SP), anti-Pitx1 (rabbit, 1:100, Novus, NBP1-88644), anti-Runx1 (rabbit, 1:200, Sigma, HPA004176), anti-Sox2 (rabbit, 1:100, Abcam, ab92492, goat, 1:100, R&D, AF2018), anti-Stard8 (rabbit, 1:50, Biorbyt, orb101873), anti-T (rabbit, 1:100, R&D, AF2085), and anti-Vimentin (rabbit, 1:200, Abcam, ab92547). The following secondary antibodies were used at 1:500: anti-goat conjugated to Alexa488 (Thermo Fisher, A20990), Cy3 (Jackson Immuno Research, AB_2307351) and 647 (Thermo Fisher A32814), anti-rabbit conjugated to Alexa488 (Thermo Fisher, A21206), and anti-rat conjugated to Alexa647 (Thermo Fisher, A21472). Alexa568 conjugated phalloidin (Invitrogen, A12380) was used at 1:200 in blocking buffer to visualize F-actin microfilaments and highlight cell membranes. Nuclei were stained with DAPI (1:1,000, Sigma, D9542).

Live imaging

For live imaging, ectoplacental cones were conserved. Embryos were cultured in 50% DMEM-F12 with L-glutamine without phenol red, 50% rat serum (Janvier), at 37°C and 5% CO_2. Embryos were observed in suspension in individual conical wells (μ-slide angiogenesis, Ibidi) to limit drift, under a Zeiss LSM 780 microscope equipped with a two-photon laser (Coherent) at 950 nm, and an LD C Apochromat 40×/ 1.1 objective. Stacks were acquired every 5 and 20 min with 5 μm Z-intervals for up to 1 h and 6 h, respectively. For short imaging, average scan increased to improve signal–noise ratio. Embryos were cultured for an additional 6–12 h after imaging to check for fitness. 3D views were processed using Arivis Vision4D v3.0 (Arivis, Germany). Registration was performed after video generation using the StackReg ImageJ plugin.

Explant live imaging and image processing

Mesoderm explants were observed under a Zeiss LSM 780 microscope equipped with an Argon laser and an LD C Apochromat 20×/0.8 objective. Stacks were acquired every 15–20 min with 3 μm Z-intervals for up to 16 h. At the end of the acquisition, explants were fixed in 4% PFA for 10 min. Manual segmentation of GFP^+ mesoderm cells was performed using Arivis Vision4D v3.0 (Arivis, Germany) on maximum Z-projections. Data analysis was performed with home-made python scripts and GraphPad (Prism).

Spectral imaging & image processing

Whole-mount fixed K8-eYFP embryos were stained with DAPI for 2 h in PBS containing 0.5% Triton X-100, 0.1% BSA, and 5% heat-inactivated horse serum. Spectral mode on Zeiss was used with a wavelength interval of 9 nm with a two-photon laser of 950 nm and a Z-interval of 1 μm. Images were unmixed through ZEN software based on prior spectral analysis of K8-eYFP and DAPI signals alone. For big samples, the Zeiss tile option was used during acquisition and unmixed images were mounted through Huygens Professional software (Deconvolution and Stitching widget).

Image quantification

Quantification from confocal images was performed using the Icy software (de Chaumont *et al*, 2012) (v2.1.0.1), ImageJ (v1.52h), and Arivis (Vision4D v3.0). Data analysis was handled through home-made Python scripts and GraphPad software (v8.4.3). Student *t*-tests or Mann–Whitney tests were used according to the nature of the data sets; ns: non-significant, **P*-value < 0.05, ***P*-value < 0.005, ****P*-value < 0.0005, and *****P*-value < 0.00005.

Electron microscopy

For Scanning Electron Microscopy, embryos were fixed with 2.5% glutaraldehyde overnight and rinsed in cacodylate buffer 0.1 M, pH 7.0. After serial dehydration in increasing concentrations of ethanol and finally acetone, samples were dried at CO_2 critical point, then opened and mounted on Scanning Electron Microscopy stubs. Observations were performed with an ESEM Quanta F200 (FEI-Thermo Fisher) microscope and secondary electron images captured with an Everhart-Thornley detector. Images were analyzed and processed by iTEM software. For Transmission Electron Microscopy analyses of thin sections, embryos were fixed with 2.5% glutaraldehyde (EM grade, Electron Microscopy Sciences) and post-fixed twice in 1% OsO4 (with 1.5% ferrocyanide). Samples were stained with uranyl acetate (UA), serially dehydrated in increasing ethanol concentrations, and embedded in epoxy resin (Agar 100 resin, Agar Scientific Ltd, UK). Sectioning was done on a Leica EM UC7 ultramicrotome and ultrathin (50–70 nm thick)

 © 2022 The Authors

sections were further stained with UA and lead citrate by electron microscopy standard procedures. Observations were made on a Tecnai 10 electron microscope (FEI-Thermo Fisher) and images were captured with a Veleta CCD camera and processed with SIS iTem software (Olympus).

Data availability

The single-cell RNA sequencing data discussed in this publication have been deposited in GEO under reference GSE167958 (http://www.ncbi.nlm.nih.gov/geo/query/acc.cgi?acc=GSE167958). A shinny application is available at https://migeottelab.shinyapps.io/ExE_Atlas_Mouse_Gastrulation/. Differential gene expression is available in Embryonic GFP positive, ExE GFP positive, allantois, amnion, chorion, and combined allantois/chorion/amnion. No graph visualization means the gene was not detected in the sample.

Expanded View for this article is available online.

Acknowledgements
We wish to thank the Université Libre de Bruxelles/Erasme animal and flow cytometry facilities. We gratefully acknowledge the Université Libre de Bruxelles light microscopy (LiMiF) core facility (M. Martens and J-M. Vanderwinden) for help with confocal and two-photon imaging, as well as the genomic facility for help with sequencing (A. Lefort and F. Libert). We thank Achim Gossler and Shankar Srinivas for sharing mouse lines, and Kirstie Lawson, Susana Chuva de Sousa Lopes, Eneko Urizar, and Joaquim Grego-Bessa for fruitful discussions. W.N. was supported by WELBIO (SGR2015), the Université Libre de Bruxelles (ULB), and the Fonds de la Recherche Scientifique (FNRS) (PDR T.0084.16). B.S. and E.D.G. received a FRIA fellowship of the FNRS. S.E.E. is supported by ASP followship from FNRS (40006730). S.P.S. is supported by the FNRS under grant number 34772792 (MISU), 40005588 (MISU-PROL), and funding from Fondation Jaumotte-Demoulin. I.M. is a FNRS research associate. The CMMI is supported by the European Regional Development Fund and the Walloon Region. S.G. acknowledges funding from FEDER Prostem Research Project no. 1510614 (Wallonia DG06), the F.R.S.-FNRS Epiforce Project no. T.0092.21 and the Interreg MAT(T)ISSE project, which is financially supported by Interreg France-Wallonie-Vlaanderen (Fonds Européen de Développement Régional, FEDER-ERDF). Work in the Magin laboratory is supported by the Deutsche Forschungsgemeinschaft (DFG), grants MA1316/19-1 and MA1316/21-2 to T.M.M. N. S. and R.E.L are supported by Deutsche Forschungsgemeinschaft (DFG) grant 363055819/GRK2415. WELBIO, the FNRS, the Fondation Jaumotte-Demoulin, and the Fonds Erasme supported this work.

Author contributions
Wallis Nahaboo: Conceptualization; Data curation; Formal analysis; Validation; Investigation; Visualization; Methodology; Writing—review and editing. **Sema Elif Eski:** Formal analysis; Visualization. **Evangéline Despin-Guitard:** Data curation; Investigation. **Marjorie Vermeersch:** Investigation; Methodology. **Marie Versaevel:** Resources; Writing—review and editing. **Bechara Saykali:** Investigation. **Daniel Monteyne:** Investigation; Methodology. **Sylvain Gabriele:** Conceptualization; Writing—review and editing. **Thomas M Magin:** Conceptualization; Resources; Writing—review and editing. **Nicole Schwarz:** Conceptualization; Resources; Writing—review and editing. **Rudolf E Leube:** Conceptualization; Resources; Writing—review and editing. **An Zwijsen:** Conceptualization; Writing—review and editing. **David Perez-Morga:** Formal analysis; Visualization; Writing—review and editing. **Sumeet Pal Singh:** Formal analysis; Methodology; Writing—review and editing. **Isabelle Migeotte:** Conceptualization; Data curation; Formal analysis; Supervision; Funding acquisition; Validation; Investigation; Writing—original draft; Project administration; Writing—review and editing.

In addition to the CRediT author contributions listed above, the contributions in detail are:

WN and IM conceptualized the study, analyzed, and interpreted data. WN performed most experiments, data quantification, and presentation. IM wrote the manuscript. SEE and SPS participated to scRNA-seq data analysis and visualization. ED-G performed immunostaining experiments. MVermeersch and DM performed the TEM and SEM experiments, MVermeersch, DM and DPM analyzed and interpreted the EM data. MVersaevel helped designing the explants experiment and made the gels. BS isolated E7.25 mesoderm cells for scRNA-seq. NS/REL and TMM provided the K8-eYFP and *Krtyll* mouse lines, respectively. NS/REL, TMM, SG and AZ were involved in conceptualization and data interpretation and reviewed the manuscript.

Disclosure and competing interests statement
The authors declare no conflict of interests.

References

Arnold SJ, Robertson EJ (2009) Making a commitment: cell lineage allocation and axis patterning in the early mouse embryo. *Nat Rev Mol Cell Biol* 10: 91 – 103

Arora R, Papaioannou VE (2012) The murine allantois: a model system for the study of blood vessel formation. *Blood* 120: 2562 – 2572

Baribault H, Price J, Miyai K, Oshima RG (1993) Mid-gestational lethality in mice lacking keratin 8. *Genes Dev* 7: 1191 – 1202

Beham A, Denk H, Desoye G (1988) The distribution of intermediate filament proteins, actin and desmoplakins in human placental tissue as revealed by polyclonal and monoclonal antibodies. *Placenta* 9: 479 – 492

Bergen V, Lange M, Peidli S, Wolf FA, Theis FJ (2020) Generalizing RNA velocity to transient cell states through dynamical modeling. *Nat Biotechnol* 38: 1408 – 1414

Bruyère C, Versaevel M, Mohammed D, Alaimo L, Luciano M, Vercruysse E, Gabriele S (2019) Actomyosin contractility scales with myoblast elongation and enhances differentiation through YAP nuclear export. *Sci Rep* 9: 15565

Burton GJ, Fowden AL, Thornburg KL (2016) Placental origins of chronic disease. *Physiol Rev* 96: 1509 – 1565

Butler A, Hoffman P, Smibert P, Papalexi E, Satija R (2018) Integrating single-cell transcriptomic data across different conditions, technologies, and species. *Nat Biotechnol* 36: 411 – 420

Chun JY, Han YJ, Ahn KY (1999) Psx homeobox gene is X-linked and specifically expressed in trophoblast cells of mouse placenta. *Dev Dyn* 216: 257 – 266

Daane JM, Downs KM (2011) Hedgehog signaling in the posterior region of the mouse gastrula suggests manifold roles in the fetal-umbilical connection and posterior morphogenesis. *Dev Dyn* 240: 2175 – 2193

Daane JM, Enders AC, Downs KM (2011) Mesothelium of the murine allantois exhibits distinct regional properties. *J Morphol* 272: 536 – 556

de Chaumont F, Dallongeville S, Chenouard N, Hervé N, Pop S, Provoost T, Meas-Yedid V, Pankajakshan P, Lecomte T, Le Montagner Y *et al* (2012) Icy: an open bioimage informatics platform for extended reproducible research. *Nat Methods* 9: 690 – 696

© 2022 The Authors

Dobreva MP, Abon Escalona V, Lawson KA, Sanchez MN, Ponomarev LC, Pereira PNG, Stryjewska A, Criem N, Huylebroeck D, de Sousa C *et al* (2018) Amniotic ectoderm expansion in mouse occurs via distinct modes and requires SMAD5-mediated signalling. *Development* 145: dev157222

Downs KM, Davies T (1993) Staging of gastrulating mouse embryos by morphological landmarks in the dissecting microscope. *Development* 118: 1255–1266

Efremova M, Vento-Tormo M, Teichmann SA, Vento-Tormo R (2020) Cell PhoneDB: inferring cell–cell communication from combined expression of multi-subunit ligand–receptor complexes. *Nat Protoc* 15: 1484–1506

Feller J, Schneider A, Schuster-Gossler K, Gossler A (2008) Noncyclic Notch activity in the presomitic mesoderm demonstrates uncoupling of somite compartmentalization and boundary formation. *Genes Dev* 22: 2166–2171

Fernandez-Gonzalez R, Simoes SM, Roper JC, Eaton S, Zallen JA (2009) Myosin II dynamics are regulated by tension in intercalating cells. *Dev Cell* 17: 736–743

Galea GL, Cho Y-J, Galea G, Molè MA, Rolo A, Savery D, Moulding D, Culshaw LH, Nikolopoulou E, Greene NDE *et al* (2017) Biomechanical coupling facilitates spinal neural tube closure in mouse embryos. *Proc Natl Acad Sci USA* 114: E5177–E5186

Grevesse T, Versaevel M, Circelli G, Desprez S, Gabriele S (2013) A simple route to functionalize polyacrylamide hydrogels for the independent tuning of mechanotransduction cues. *Lab Chip* 13: 777–780

Guillemot F, Nagy A, Auerbach A, Rossant J, Joyner AL (1994) Essential role of Mash-2 in extraembryonic development. *Nature* 371: 333–336

Guo D-C, Pannu H, Tran-Fadulu V, Papke CL, Yu RK, Avidan N, Bourgeois S, Estrera AL, Safi HJ, Sparks E *et al* (2007) Mutations in smooth muscle alpha-actin (ACTA2) lead to thoracic aortic aneurysms and dissections. *Nat Genet* 39: 1488–1493

Gurtner GC, Davis V, Li H, McCoy MJ, Sharpe A, Cybulsky MI (1995) Targeted disruption of the murine VCAM1 gene: essential role of VCAM-1 in chorioallantoic fusion and placentation. *Genes Dev* 9: 1–14

Hesse M, Franz T, Tamai Y, Taketo MM, Magin TM (2000) Targeted deletion of keratins 18 and 19 leads to trophoblast fragility and early embryonic lethality. *Embo J* 19: 5060–5070

Hoffmann I, Balling R (1995) Cloning and expression analysis of a novel mesodermally expressed cadherin. *Dev Biol* 169: 337–346

Inman KE, Downs KM (2006) Brachyury is required for elongation and vasculogenesis in the murine allantois. *Development* 133: 2947–2959

Inman KE, Downs KM (2007) The murine allantois: emerging paradigms in development of the mammalian umbilical cord and its relation to the fetus. *Genesis* 45: 237–258

Khong TY, Lane EB, Robertson WB (1986) An immunocytochemical study of fetal cells at the maternal-placental interface using monoclonal antibodies to keratins, vimentin and desmin. *Cell Tissue Res* 246: 189–195

Krawetz R, Kelly GM (2008) Wnt6 induces the specification and epithelialization of F9 embryonal carcinoma cells to primitive endoderm. *Cell Signal* 20: 506–517

La Manno G, Soldatov R, Zeisel A, Braun E, Hochgerner H, Petukhov V, Lidschreiber K, Kastriti ME, Lönnerberg P, Furlan A *et al* (2018) RNA velocity of single cells. *Nature* 560: 494–498

Laly AC, Sliogeryte K, Pundel OJ, Ross R, Keeling MC, Avisetti D, Waseem A, Gavara N, Connelly JT (2021) The keratin network of intermediate filaments regulates keratinocyte rigidity sensing and nuclear mechanotransduction. *Sci Adv* 7: 1–12

Latorre E, Kale S, Casares L, Gómez-González M, Uroz M, Valon L, Nair RV, Garreta E, Montserrat N, del Campo A *et al* (2018) Active superelasticity in three-dimensional epithelia of controlled shape. *Nature* 563: 203–208

Li S, Roberson MS (2017) DLX3 interacts with GCM1 and inhibits its transactivation-stimulating activity in a homeodomain-dependent manner in human trophoblast-derived cells. *Sci Rep* 7: 1–13

Lim HYG, Alvarez YD, Gasnier M, Wang Y, Tetlak P, Bissiere S, Wang H, Biro M, Plachta N (2020) Keratins are asymmetrically inherited fate determinants in the mammalian embryo. *Nature* 585: 404–409

Loschke F, Seltmann K, Bouameur JE, Magin TM (2015) Regulation of keratin network organization. *Curr Opin Cell Biol* 32: 56–64

Lu H, Hesse M, Peters B, Magin TM (2005) Type II keratins precede type I keratins during early embryonic development. *Eur J Cell Biol* 84: 709–718

Manohar S, Camacho-Magallanes A, Echeverria C, Rogers CD (2020) Cadherin-11 is required for neural crest specification and survival. *Front Physiol* 11: 563372

Marsh B, Blelloch R (2020) Single nuclei RNA-seq of mouse placental labyrinth development. *Elife* 9: 1–27

Martin P, Lewis J (1992) Actin cables and epidermal movement in embryonic wound healing. *Nature* 360: 179–183

Matoba S, Nakamuta S, Miura K, Hirose M, Shiura H, Kohda T, Nakamuta N, Ogura A (2019) Paternal knockout of Slc38a4/SNAT4 causes placental hypoplasia associated with intrauterine growth restriction in mice. *Proc Natl Acad Sci USA* 116: 21047–21053

Moch M, Schwarz N, Windoffer R, Leube RE (2020) The keratin–desmosome scaffold: pivotal role of desmosomes for keratin network morphogenesis. *Cell Mol Life Sci* 77: 543–558

Morasso MI, Grinberg A, Robinson G, Sargent TD, Mahon KA (1999) Placental failure in mice lacking the homeobox gene Dlx3. *Proc Natl Acad Sci USA* 96: 162–167

Muzumdar MD, Tasic B, Miyamichi K, Li L, Luo L (2007) A global double-fluorescent Cre reporter mouse. *Genesis* 45: 593–605

Nahaboo W, Migeotte I (2018) Cleavage and gastrulation in the mouse embryo. In *eLS*, pp. 1–6. Chichester: John Wiley & Sons, Ltd. https://doi.org/10.1002/9780470015902.a0001068.pub3

Nandadasa S, Szafron JM, Pathak V, Murtada S-I, Kraft CM, O'Donnell A, Norvik C, Hughes C, Caterson B, Domowicz MS *et al* (2020) Vascular dimorphism ensured by regulated proteoglycan dynamics favors rapid umbilical artery closure at birth. *Elife* 9: 1–30

Nieto MA, Gilardi-Hebenstreit P, Charnay P, Wilkinson DG (1992) A receptor protein tyrosine kinase implicated in the segmental patterning of the hindbrain and mesoderm. *Development* 116: 1137–1150

Noll B, Benz D, Frey Y, Meyer F, Lauinger M, Eisler SA, Schmid S, Hordijk PL, Olayioye MA (2019) DLC3 suppresses MT1-MMP-dependent matrix degradation by controlling RhoB and actin remodeling at endosomal membranes. *J Cell Sci* 132: jcs223172

Nowotschin S, Setty M, Kuo Y-Y, Liu V, Garg V, Sharma R, Simon CS, Saiz N, Gardner R, Boutet SC *et al* (2019) The emergent landscape of the mouse gut endoderm at single-cell resolution. *Nature* 569: 361–367

Ockleford C, Malak T, Hubbard A, Bracken K, Burton SA, Bright N, Blakey G, Goodliffe J, Garrod D, d'Lacey C (1993) Confocal and conventional immunofluorescence and ultrastructural localisation of intracellular strength-giving components of human amniochorion. *J Anat* 183: 483–505

Parr BA, Cornish VA, Cybulsky MI, McMahon AP (2001) Wnt7b regulates placental development in mice. *Dev Biol* 237: 324–332

Pereira PN, Dobreva MP, Graham L, Huylebroeck D, Lawson KA, Zwijsen A (2011) Amnion formation in the mouse embryo: the single amniochorionic fold model. *BMC Dev Biol* 11: 48

Perez-Garcia V, Fineberg E, Wilson R, Murray A, Mazzeo CI, Tudor C, Sienerth A, White JK, Tuck E, Ryder EJ *et al* (2018) Placentation defects are highly prevalent in embryonic lethal mouse mutants. *Nature* 555: 463–468

 © 2022 The Authors

Pijuan-Sala B, Griffiths JA, Guibentif C, Hiscock TW, Jawaid W, Calero-Nieto FJ, Mulas C, Ibarra-Soria X, Tyser RCV, Ho DLL *et al* (2019) A single-cell molecular map of mouse gastrulation and early organogenesis. *Nature* 566: 490 – 495

Pittet P, Lee K, Kulik AJ, Meister JJ, Hinz B (2008) Fibrogenic fibroblasts increase intercellular adhesion strength by reinforcing individual OB-cadherin bonds. *J Cell Sci* 121: 877 – 886

Pora A, Yoon S, Dreissen G, Hoffmann B, Merkel R, Windoffer R, Leube RE (2020) Regulation of keratin network dynamics by the mechanical properties of the environment in migrating cells. *Sci Rep* 10: 1 – 17

Ramms L, Fabris G, Windoffer R, Schwarz N, Springer R, Zhou C, Lazar J, Stiefel S, Hersch N, Schnakenberg U *et al* (2013) Keratins as the main component for the mechanical integrity of keratinocytes. *Proc Natl Acad Sci USA* 110: 18513 – 18518

Roberts RM, Green JA, Schulz LC (2016) The evolution of the placenta. *Reproduction* 152: R179 – R189

Rossant J, Cross JC (2001) Placental development: lessons from mouse mutants. *Nat Rev Genet* 2: 538 – 548

Sanghvi-Shah R, Weber GF (2017) Intermediate filaments at the junction of mechanotransduction, migration, and development. *Front Cell Dev Biol* 5: 1 – 19

Saykali B, Mathiah N, Nahaboo W, Racu M-L, Hammou L, Defrance M, Migeotte I (2019) Distinct mesoderm migration phenotypes in extra-embryonic and embryonic regions of the early mouse embryo. *Elife* 8: e42434

Schlegel N, Meir M, Heupel W-M, Holthöfer B, Leube RE, Waschke J (2010) Desmoglein 2-mediated adhesion is required for intestinal epithelial barrier integrity. *Am J Physiol Liver Physiol* 298: G774 – G783

Schmidt C, Stoeckelhuber M, McKinnell I, Putz R, Christ B, Patel K (2004) Wnt 6 regulates the epithelialisation process of the segmental plate mesoderm leading to somite formation. *Dev Biol* 271: 198 – 209

Schwarz N, Windoffer R, Magin TM, Leube RE (2015) Dissection of keratin network formation, turnover and reorganization in living murine embryos. *Sci Rep* 5: 1 – 8

Seltmann K, Fritsch AW, Käs JA, Magin TM (2013) Keratins significantly contribute to cell stiffness and impact invasive behavior. *Proc Natl Acad Sci USA* 110: 18507 – 18512

Shapland C, Hsuan JJ, Totty NF, Lawson D (1993) Purification and properties of transgelin: a transformation and shape change sensitive actin-gelling protein. *J Cell Biol* 121: 1065 – 1073

Simmons DG, Natale DRC, Begay V, Hughes M, Leutz A, Cross JC (2008) Early patterning of the chorion leads to the trilaminar trophoblast cell structure in the placental labyrinth. *Development* 135: 2083 – 2091

Smedley D, Haider S, Ballester B, Holland R, London D, Thorisson G, Kasprzyk A (2009) BioMart - biological queries made easy. *BMC Genom* 10: 1 – 12

Soares MJ, Varberg KM, Iqbal K (2018) Hemochorial placentation: development, function, and adaptations. *Biol Reprod* 99: 196 – 211

Sonavane PR, Wang C, Dzamba B, Weber GF, Periasamy A, DeSimone DW (2017) Mechanical and signaling roles for keratin intermediate filaments in the assembly and morphogenesis of mesendoderm tissue at gastrulation. *Development* 44: 4363 – 4376

Srinivas S, Rodriguez T, Clements M, Smith JC, Beddington RSP (2004) Active cell migration drives the unilateral movements of the anterior visceral endoderm. *Development* 131: 1157 – 1164

Suryawanshi H, Morozov P, Straus A, Sahasrabudhe N, Max KEA, Garzia A, Kustagi M, Tuschl T, Williams Z (2018) A single-cell survey of the human first-trimester placenta and decidua. *Sci Adv* 4: 1 – 13

Tamai Y, Ishikawa TO, Bösl MR, Mori M, Nozaki M, Baribault H, Oshima RG, Taketo MM (2000) Cytokeratins 8 and 19 in the mouse placental development. *J Cell Biol* 151: 563 – 572

Tyser RCV, Mahammadov E, Nakanoh S, Vallier L, Scialdone A, Srinivas S (2021) Single-cell transcriptomic characterization of a gastrulating human embryo. *Nature* 600: 285 – 289

Vento-Tormo R, Efremova M, Botting RA, Turco MY, Vento-Tormo M, Meyer KB, Park J-E, Stephenson E, Polański K, Goncalves A *et al* (2018) Single-cell reconstruction of the early maternal–fetal interface in humans. *Nature* 563: 347 – 353

Vijayaraj P, Kröger C, Reuter U, Windoffer R, Leube RE, Magin TM (2009) Keratins regulate protein biosynthesis through localization of GLUT1 and -3 upstream of AMP kinase and Raptor. *J Cell Biol* 187: 175 – 184

Vijayaraj P, Kroeger C, Reuter U, Hartmann D, Magin TM (2010) Keratins regulate yolk sac hematopoiesis and vasculogenesis through reduced BMP-4 signaling. *Eur J Cell Biol* 89: 299 – 306

Watson ED, Cross JC (2005) Development of structures and transport functions in the mouse placenta. *Physiology (Bethesda)* 20: 180 – 193

Weber GF, Bjerke MA, DeSimone DW (2012) A mechanoresponsive cadherin-keratin complex directs polarized protrusive behavior and collective cell migration. *Dev Cell* 22: 104 – 115

Yang JT, Rayburn H, Hynes RO (1995) Cell adhesion events mediated by α4 integrins are essential in placental and cardiac development. *Development* 121: 549 – 560

Yang R, Goedel A, Kang Y, Si C, Chu C, Zheng Y, Chen Z, Gruber PJ, Xiao Y, Zhou C *et al* (2021) Amnion signals are essential for mesoderm formation in primates. *bioRxiv*. https://doi.org/10.1038/s41467-021-25186-2

Yoon S, Leube RE (2019) Keratin intermediate filaments: intermediaries of epithelial cell migration. *Essays Biochem* 63: 521 – 533

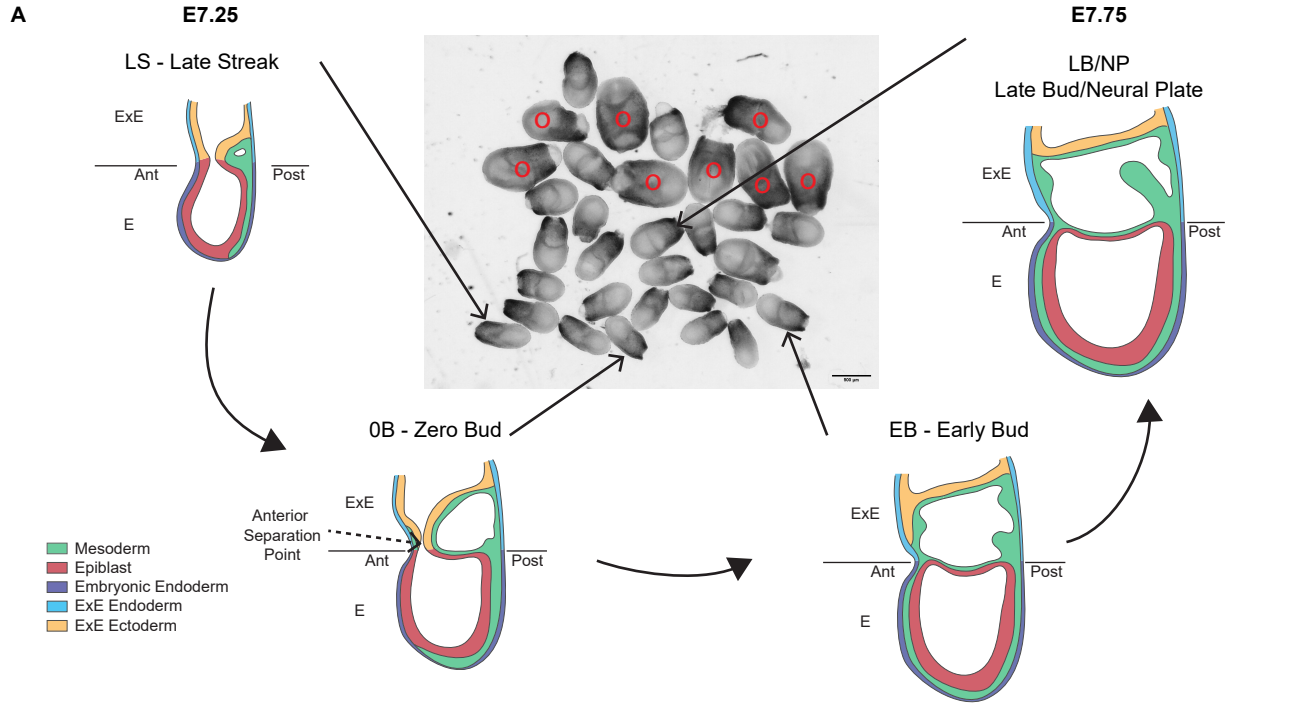
© 2022 The Authors

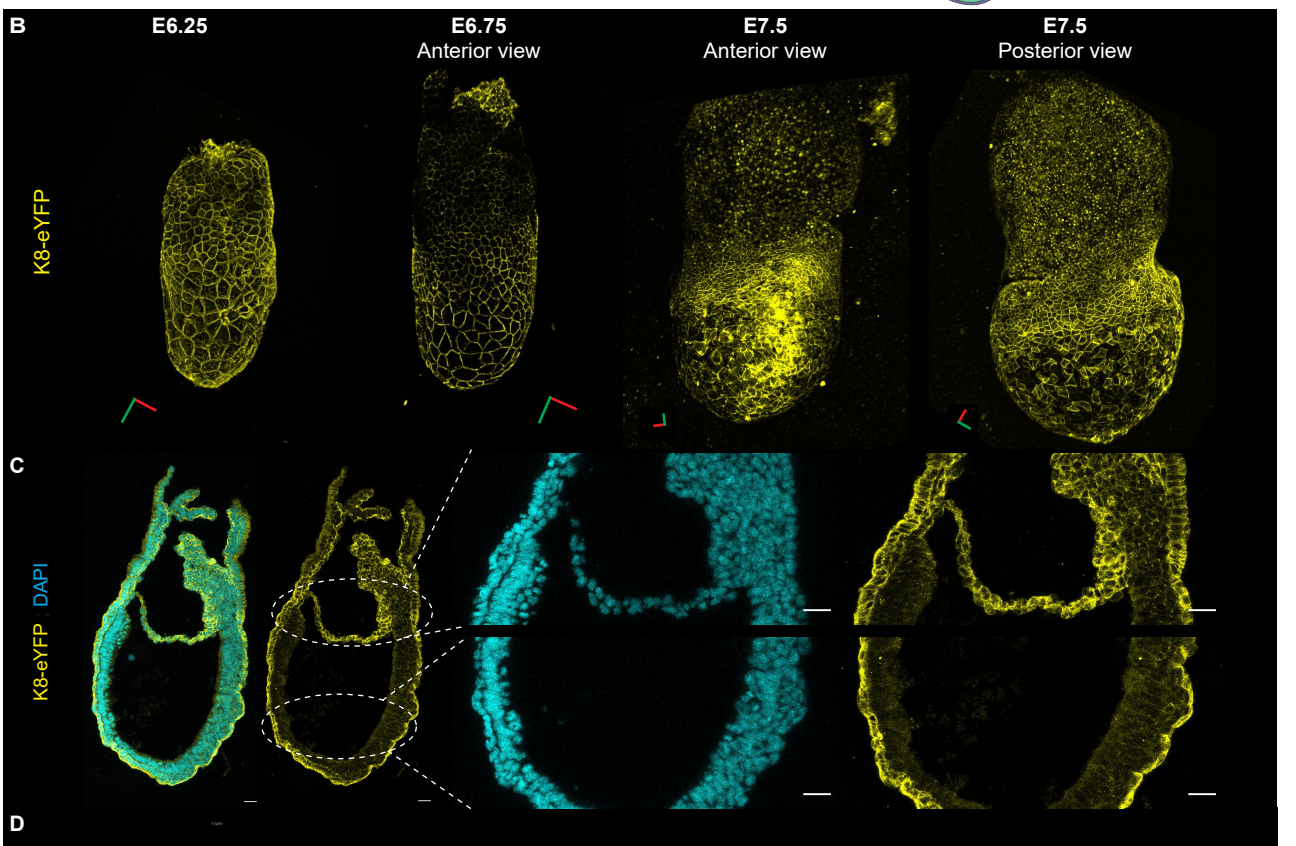
Appendix Table of Contents:

Appendix Figure S1: **Embryo staging and cytoskeletal markers**

Appendix Figure S2: Embryonic and ExE mesoderm single cell transcriptome

Appendix Figure S1







Appendix Figure S1: **Embryo staging and cytoskeletal markers**

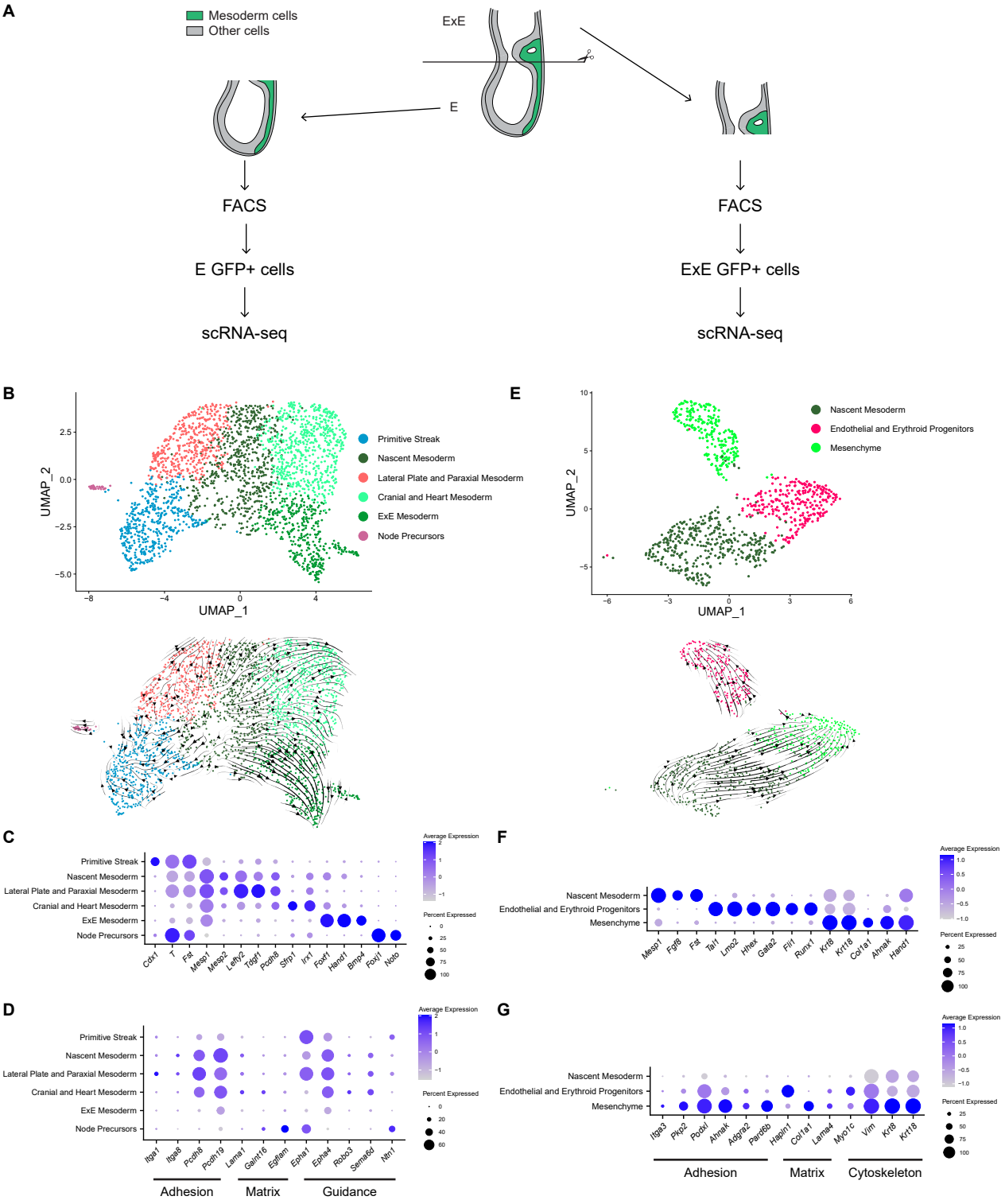
A. Classification of embryos as Late Streak (LS), Zero Bud (0B), Early Bud (EB), and Late Bud/Neural Plate (LB/NP) stages based on bright-field image of two litters dissected at late E7.5. Head Folds stage embryos (red circles) were not used for live imaging. Data information: Scale bar represents 500 μm.

B. 3D reconstructions from two-photon stacks of fixed K8-eYFP embryo dissected at E6.25, E6.75, E7.5 showing visceral endoderm labelling. Green and red bars represent 40 μm in the X and Y axis, respectively.

C. Z-projections of sagittal sections from a LB K8-eYFP embryo (n=30) with zooms (white dashed circles) on embryonic (Bottom) and ExE (Top) regions showing expression in endoderm as well as ExE ectoderm and mesoderm. K8-eYFP and DAPI appear in yellow and cyan, respectively. Scale bars represent 25 μm.

D. 3D reconstructions of whole-mount LB embryo stained for F-actin (Phalloidin, red). Grid squares represent 200 μm.

Appendix Figure S2



Appendix Figure S2: Embryonic and ExE mesoderm single cell transcriptome

A. Strategy for isolation of mesoderm cells from M/LS mTmG; *T*-Cre embryos. Embryos were cut manually at the embryonic/ExE border and GFP positive cells were sorted by flow cytometry.

B. UMAP (Top) and RNA velocity (Bottom) of embryonic mesoderm cells where 6 unsupervised clusters were identified.

C. Dot plot of specific gene expression in clusters in the embryonic region.

D. Dot plot of genes previously found to have higher expression in embryonic, compared to ExE, mesoderm with roles in adhesion (*Itga1*, *Itga8*, *Pcdh9*, *Pcdh19*), matrix (*Lama1*, *Galnt16*, *Egflam*), and guidance (*Epha1*, *Epha4*, *Robo3*, *Sema6d*, *Ntn1*).

E. UMAP (Top) and RNA velocity (Bottom) of ExE mesoderm cells where 3 unsupervised clusters were identified.

F. Dot plot of specific gene expression in clusters in ExE region.

G. Dot plot of genes previously found to have higher expression in ExE, compared to embryonic, mesoderm with roles in adhesion (*Itga3*, *Pkp2*, *Podxl*, *Ahnak, Pard6b*), matrix (*Hapln1*, *Col1a1*, *Lama4*), and cytoskeleton (*Myoc1c*, *Vim*, *Krt8*, *Krt18*).